UNIVERSITÀ
DEGLI STUDI
DI PADOVA

DIPARTIMENTO
DI INGEGNERIA
DELL'INFORMAZIONE

UNIVERSITY OF PADUA
DEPARTMENT OF INFORMATION ENGINEERING

MASTER'S DEGREE IN ELECTRONIC ENGINEERING

Study of very-high-energy beams for single-event effects testing of electronic devices

Supervisor: Prof. Gerardin Simone

Candidate: Sorgato Riccardo
Student ID: 2097147

Co-supervisor: Prof. Bagatin Marta

ACADEMIC YEAR 2025 – 2026

Graduation date: 14/04/2026

Abstract

This thesis develops a Geant4/GRAS simulation workflow to interpret heavy-ion deposited-energy spectra measured with a silicon PIPS diode within the HEARTS beam-quality campaigns at CERN IRRAD (Pb-208) and at GSI Cave A (U-238). The central idea is that, for SEE-related measurements in very-high-energy heavy-ion environments, the relevant quantity is not the nominal beam settings alone, but the effective particle field at the device under test (DUT) after transport through degraders, upstream materials, and detector/package geometry.

To address this problem, a detailed GDML model of the detector and its package is implemented to account for multiple trajectory families, including ions entering through the front aperture and ions crossing additional package materials. An upstream scoring plane is used to define the beam energy at the DUT consistently, enabling a quantitative mapping between degrader thickness and residual energy, together with a characterization of energy-loss straggling. Deposited-energy spectra are then analyzed across configurations and compared with the experimental HEARTS reference data. The simulations reproduce the main spectral topologies over a broad range of beam conditions and show an increased sensitivity to trajectory selection, transmission, and material-budget details in the near-stopping regime.

In addition, a complementary TCAD study (Synopsys Sentaurus) is carried out on a 300-µm reverse-biased PIN diode to investigate the intrinsic current generated by a LET-parametrized ionization event. Comparison with CERN waveform data shows partial consistency in the onset and peak region, while the longer experimental decay is not reproduced by the intrinsic device response alone. Overall, the work shows that meaningful interpretation of VHE SEE measurements requires both transport-level and device-level analysis.

Contents

Chapter 1 – Introduction

1.1 Motivation: SEE testing with very-high-energy beams

Single-event effects (SEE) represent a key reliability concern for electronic devices operating in radiation environments. Unlike other cumulative degradation mechanisms, SEE are triggered by individual particles and therefore occur stochastically, potentially leading to transient malfunctions or, in the worst case, destructive events. For this reason, SEE qualification relies on controlled ground-based irradiation campaigns. By exposing devices under test (DUTs) to particle beams under monitored conditions, it is possible to observe failure modes under representative operating states and derive quantitative metrics used for engineering decisions [1] [2].

In this context, the relevant test condition is not only defined by the nominal accelerator settings, but by the effective particle field that reaches the DUT after traversing the full upstream material budget (beamline elements, windows, air gaps etc.) and the DUT packaging [3] [4].

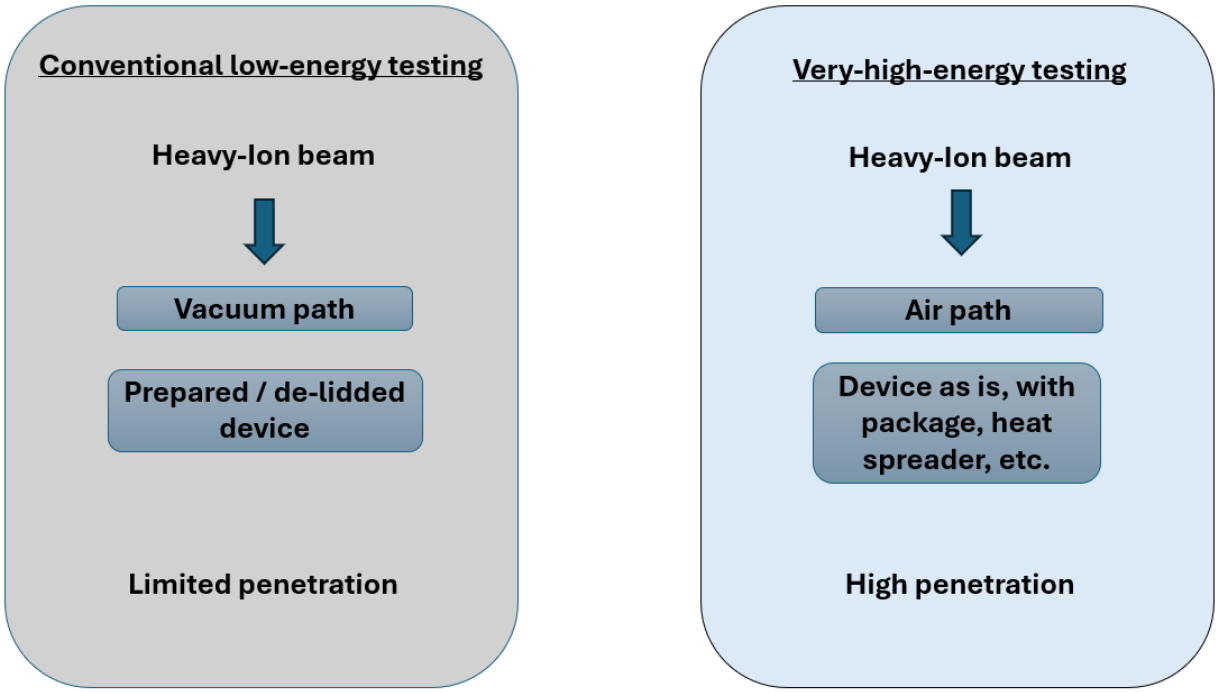

Figure 1: Conceptual comparison between conventional low-energy and very-high-energy heavy-ion testing.

Very-high-energy (VHE) heavy-ion beams are particularly interesting for modern SEE testing. Compared to conventional heavy-ion testing at lower energies, VHE ions exhibit higher penetration, enabling irradiation scenarios that are closer to system-level conditions [3].

At the same time, VHE testing introduces additional complexity: particles may traverse more material before reaching sensitive regions, energy-loss straggling can broaden the residual-energy distribution, and nuclear interactions in the crossed materials can generate secondary particles that further modify the field at the DUT [4]. As a consequence, the VHE beams used for SEE testing require dedicated beam characterization methods and, often, simulation support to interpret measured observables in the presence of realistic geometry and material stacks.

In the following sections, these motivations are linked to the need for beam characterization and to the broader framework of the HEARTS project, where deposited-energy spectra measured with silicon diodes are used to assess beam quality at different infrastructures and settings, and where comparison with simulations is part of the interpretation strategy [5] [6].

1.2 Why "beam characterization" is a prerequisite

In SEE irradiation campaigns, the experimental outcome is only meaningful if the radiation field impacting on the device under test (DUT) is sufficiently known, stable, and reproducible. In practice, this requirement goes beyond reporting nominal accelerator parameters: for quantitative interpretation, the relevant quantity is the effective particle field at the DUT [2] (what actually arrives at the DUT plane after all upstream materials and geometrical constraints have shaped the beam).

A "well-characterized" beam, in the operational sense needed for SEE testing, therefore implies [5]:

I. knowledge of the particle composition at the DUT, including possible secondary fragments
II. knowledge of the energy and angular distributions
III. control of time stability and reproducibility across runs

This prerequisite is particularly stringent for very-high-energy (VHE) heavy ions, where upstream degraders, windows, air gaps, and mechanical fixtures can introduce energy-loss straggling and additional secondary particle production, making the DUT field more complex than the nominal beam label suggests [4].

Within the HEARTS project, beam-quality validation at CERN and GSI is addressed through measurements of deposited-energy spectra in a silicon PIPS diode (by Mirion), a reverse-biased silicon diode detector used as a spectroscopic diagnostic, using deposited-energy spectra as an observable to analyze beam conditions. The idea is that the deposited-energy distribution is sensitive not only to the ion species and residual energy, but also to the effective material stack and acceptance that particles experience before reaching the sensitive volume, so it naturally captures "what the DUT would see" in a setup-dependent way [5] [7].

Figure 2: Picture of one of the PIPS diodes used for heavy-ion beam characterization, shown in top, bottom, and side views. The stainless-steel package and the front aperture above the active area are visible. Reproduced from [6].

However, the same sensitivity that makes deposited-energy spectra valuable also implies that their interpretation is not always straightforward. Multiple trajectory classes through a realistic detector/package geometry, together with straggling and fragmentation effects, can generate multiple spectral structures that cannot be unambiguously attributed to beam parameters only by inspection. For this reason, characterization measurements are most effective when coupled to detailed modeling, so that geometry and materials can be accounted for consistently and diagnostic observables can be interpreted quantitatively rather than qualitatively [7].

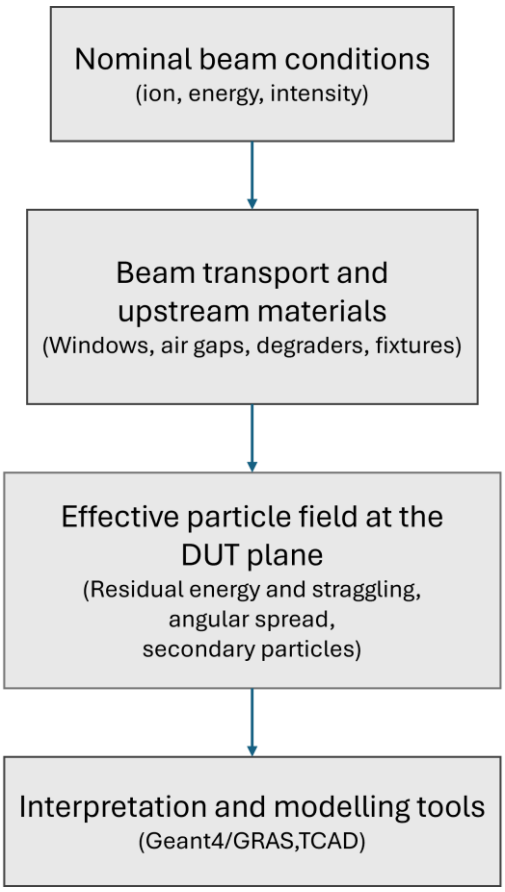

Figure 3: From nominal beam conditions to the effective particle field at the DUT

In this thesis, this prerequisite motivates the modeling approach adopted in the technical chapters. In Chapter 3 and 4, Geant4/GRAS transport simulations are used to reproduce and interpret the deposited-energy spectra measured with a PIPS diode in the HEARTS beam-quality campaigns, using a detailed detector-package geometry described in GDML and a consistent analysis workflow. In Chapter 5, TCAD simulations (Sentaurus) are used to model the transient response of a PIN-like diode under ionization conditions parameterized by the Linear Energy Transfer (LET), complementing the beam-level picture with a device-level description of signal formation and providing a framework for comparison with transient datasets acquired at CERN.

1.3 HEARTS context

The High-Energy Accelerators for Radiation Testing and Shielding (HEARTS) project is an EU-funded initiative running from January 2023 to December 2026. It aims to improve European

facilities and procedures for radiation testing of electronics by enabling the use of high-energy heavy-ion beams for space-related applications [6].

A key idea behind HEARTS is that high-energy ions (above 100 MeV/n) can better penetrate materials and therefore support more realistic test conditions, for example irradiation in air and testing at higher assembly levels. This approach can also reduce the need for device preparation steps such as de-lidding or thinning in some test scenarios [3] [6].

In HEARTS, CERN and GSI act as accelerator infrastructure partners supporting the development of these high-energy heavy-ion testing capabilities. The consortium also includes the University of Padua as an academic partner and industrial participants (Thales Alenia Space and Airbus Defence and Space), who contribute by defining technical and procedural requirements for VHE-ion user facilities. These requirements are then implemented as facility upgrades and validated through "real case" experimental campaigns, which also provide input for recommendations and guidelines for VHE-ion testing.

1.4 Objectives and contributions

This thesis is developed within the HEARTS framework and focuses on the interpretation of PIPS-diode deposited-energy measurements through dedicated Monte Carlo transport simulations and analysis tools.

The first point of this work is to build a Geant4/GRAS simulation setup able to reproduce the experimental conditions and to support the interpretation of the measured spectra. In particular, the same detector-package geometry and analysis workflow are used across different facilities and beam settings, so that differences in the spectra can be connected to changes in beam conditions rather than to changes in the model itself.

The second point is to complement the Monte Carlo analysis with TCAD simulations (Synopsys Sentaurus) used to model the transient current response of a reverse-biased PIN-like diode after a heavy-ion ionization event parameterized by LET. In this way, the thesis extends the interpretation from deposited-energy observables to the device-level formation of transient signals.

The main contributions of this thesis are:

- A GDML-based model of the PIPS detector and its package, suitable for studying path-dependent energy losses (ex. trajectories through the aperture versus through additional package layers).

- A consistent Geant4/GRAS workflow to score the beam energy upstream of the detector and to generate event-by-event deposited-energy spectra for comparison across configurations and facilities.
- A method to relate degrader settings to the effective energy at the detector entrance, enabling comparisons at equivalent DUT energies instead of relying only on nominal settings.
- A complementary TCAD setup for transient simulations of a PIN diode under heavy-ion ionization, used to study device-level signal formation and compare simulated trends with experimental transient waveforms.

Chapter 2 – Background

2.1 Single-event effects: definitions and test philosophy

As introduced in the first chapter, Single-Event Effects (SEE) are degradation mechanisms in electronic devices caused by a single ionizing particle interaction (or by its secondary products) that produces a localized ionization in a sensitive region of the device. Depending on the device technology and operating conditions, this localized charge deposition may result in a transient perturbation, a change of state, or, in some cases, a permanent failure mechanism [8].

SEE are commonly classified into non-destructive and potentially destructive categories.

Typical non-destructive effects include Single-Event Upset (SEU), for example a bit flip in a memory element, and Single-Event Transient (SET), a transient pulse in combinational logic or analog nodes that may be latched by subsequent stages [8].

Potentially destructive effects include, for example, Single-Event Latchup (SEL), Single-Event Burnout (SEB), and Single-Event Gate Rupture (SEGR), which can lead to abnormal high-current conditions or permanent damage if not properly mitigated.

From a test and qualification perspective, SEE sensitivity is typically summarized through a cross section as a function of Linear Energy Transfer (LET), providing a link between the ionizing strength of the incident particle and the probability of observing a given effect [9].

Key parameters often discussed in this context include the threshold LET for the onset of events and the saturation cross section at high LET, which are then used to support engineering decisions and to estimate SEE rates in the target radiation environment [8].

2.2 VHE heavy-ion beams vs conventional testing

Very-high-energy (VHE) heavy-ion irradiation setups operate in a regime where particles can go through non-negligible material thicknesses before reaching the region of interest, making the particle-matter interaction mechanisms central to the interpretation of test conditions and diagnostics [3] [10].

For charged heavy particles, the electronic energy loss in matter (stopping power) is described by the Bethe equation, which captures the dominant dependence on the projectile charge and velocity through an overall z^2/β^2 scaling and a slowly varying logarithmic term.

When the ion slows down, the stopping power increases and the energy deposition tends to become more concentrated toward the end of the track, leading to the well known “Bragg-like” behavior that links penetration depth to LET (or, more generally, to $-dE/dx$). In practical terms, this implies that the ionizing strength experienced by a device can be strongly depth-dependent when the beam energy is reduced close to a stopping regime, even if the incident ion species is unchanged [10].

Besides the mean energy loss, event-by-event fluctuations in energy loss, usually referred to as energy-loss straggling, are intrinsic to ionization processes and become particularly relevant in thin layers and in situations where only a limited number of collisions contribute to the total deposited-energy. For detector-like thicknesses, the energy-deposit distribution of a single particle is generally asymmetric and is often described by Landau or Landau -Vavilov type distributions, making the most probable energy loss a more robust descriptor than the mean in many spectroscopy-like measurements.

These fluctuations, together with any additional upstream energy-degrading material, naturally broaden the residual-energy distribution of the particles and therefore can broaden deposited-energy observables measured in silicon. A further key effect is angular broadening due to multiple Coulomb scattering, (the accumulation of many small angle deflections on nuclei as the particle traverses matter). In the central part of the distribution the net deflection can be approximated as Gaussian, while less frequent hard scatters contribute to non-Gaussian tails. In irradiation geometries with apertures, collimation, or compact detector packages, multiple scattering can change the effective acceptance and the path-length distribution through different materials, therefore linking beam transport to geometry in a non-trivial way [11].

Finally, rare hard collisions can also produce energetic secondary electrons (δ rays), which carry away a non-negligible fraction of the transferred energy and modify the spatial pattern of energy deposition around the primary track. For hadronic projectiles, nuclear interactions may provide an additional contribution, making a pure range-based picture less complete when nuclear interaction lengths become comparable with the crossed material budget.

The combined action of mean stopping power, straggling, and multiple scattering explains why upstream materials and geometry can reshape the particle field at the DUT and, consequently, the deposited-energy response of a silicon diagnostic detector. This is the physical basis for the more operational discussion of degraders introduced in the next section [10].

2.2.1 Stopping power and range (Bragg curve, CSDA, limitations)

Charged particles such as protons and heavy ions lose kinetic energy in matter mainly through ionization, and this energy loss is commonly described in terms of stopping power and Linear Energy Transfer (LET). In the context of this thesis, these concepts provide the physical basis for using SRIM stopping/range tables as an external check on whether ions in each beam configuration are expected to penetrate specific package layers and reach the 300-µm sensitive silicon region [10] [12].

The Bragg curve is here intended as the depth dependence of the stopping power, or of the energy loss per unit path length (-dE/dx), for a charged particle slowing down in a medium. Its characteristic shape arises because, as the projectile slows down, the stopping power increases and the energy loss becomes progressively larger. In simplified terms, the energy loss depends strongly on the projectile charge and velocity, and this leads to a pronounced maximum close to the end of the track. This maximum is the Bragg peak, which occurs at low energies just before the projectile stops. Operationally, the presence of a peak near the end of range is what makes the notion of "range" useful: small changes in the upstream material budget can move a subset of ions closer to (or beyond) their stopping point, producing large changes in the residual energy entering a downstream layer. This sensitivity is exactly what is exploited in this thesis when interpreting, in a qualitative but still quantitative way, the appearance or suppression of spectral components associated with different trajectory families through the PIPS package [10].

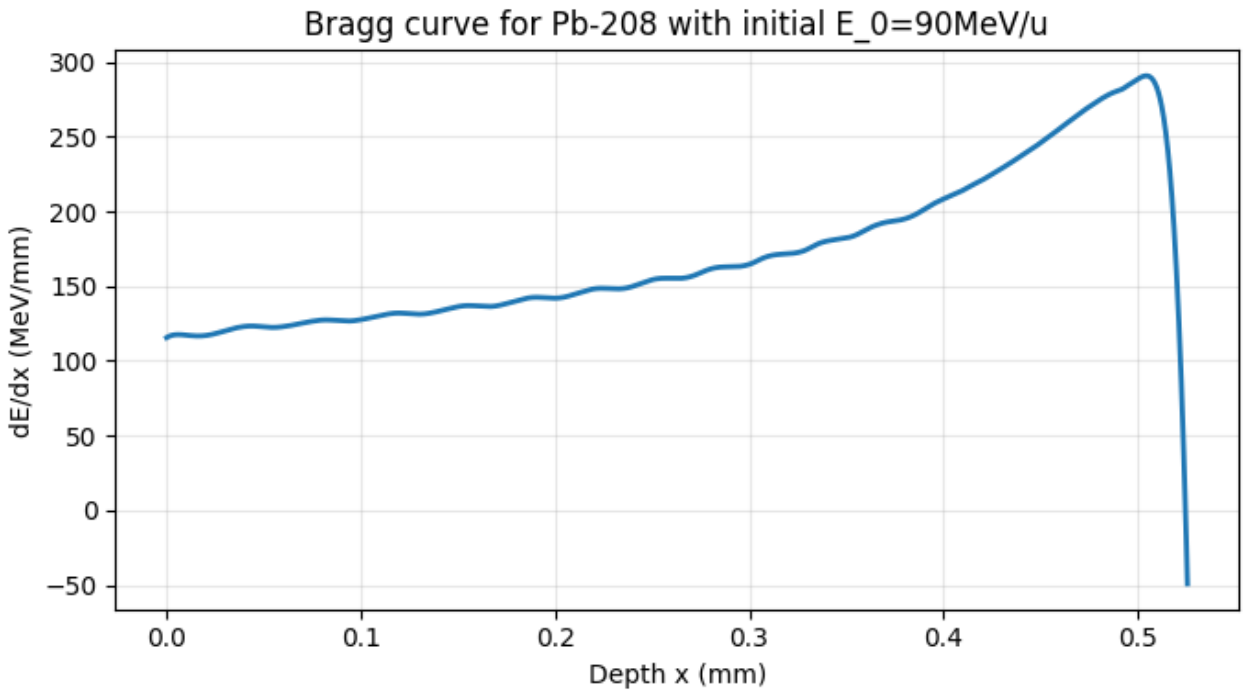

Figure 4: Bragg curve calculated using SRIM [12], for Lead ions with an initial energy of 90MeV/u.

To connect stopping power to a penetration depth, the continuous slowing down approximation (CSDA) is commonly used. The CSDA range is a close approximation to the average distance traveled by a charged particle as it slows down to rest when the energy loss rate along the track is taken equal to the total stopping power and energy-loss fluctuations are neglected. In this approximation, the range is obtained by integrating the reciprocal of the total stopping power with respect to energy, providing a deterministic relation between kinetic energy and mean residual path length in a given material [10].

SRIM stopping/range tables provide a practical implementation of this relation for specific ion-material pairs. In the layer-by-layer study presented in this thesis, this is applied to the main materials in the GDML-defined detector stack (stainless steel, elastomer, polymer, aluminum, and silicon) to estimate energy degradation and, whether the primary ion is expected to reach the active silicon for different representative paths.

It is important to state the limitations of this approach. Since CSDA neglects energy-loss fluctuations (straggling) and does not model angular scattering, SRIM-based layer-by-layer propagation should be interpreted as a mean, 1D penetration estimate rather than an event-by-event prediction. For heavy ions, additional effects such as nuclear fragmentation in degraders can

modify the depth LET profile and produce tails in Bragg curves, further motivating the use of SRIM here as a complementary cross-check rather than a standalone spectral model [12].

2.3 Degraders and fragmentation effects: shaping a particle field at the DUT

Within the particle-matter interaction mechanisms introduced in Section 2.2, upstream material (beamline windows, air gaps, degraders, detector/package layers) can reshape the particle field at the DUT by modifying not only the mean energy but also the energy spread, angular distribution, and, in some cases, the particle composition through nuclear interactions [10].

For this reason, it is useful to distinguish between energy-degrading effects (mainly driven by electromagnetic interactions) and fragmentation effects (driven by nuclear reactions), since the two mechanisms impact diagnostics and test interpretation in different ways.

A degrader is an absorber of controlled thickness inserted upstream of the DUT to reduce the residual energy of the primary ions (which are the original ions of the incident beam before any secondary fragmentation) through the electronic stopping force.

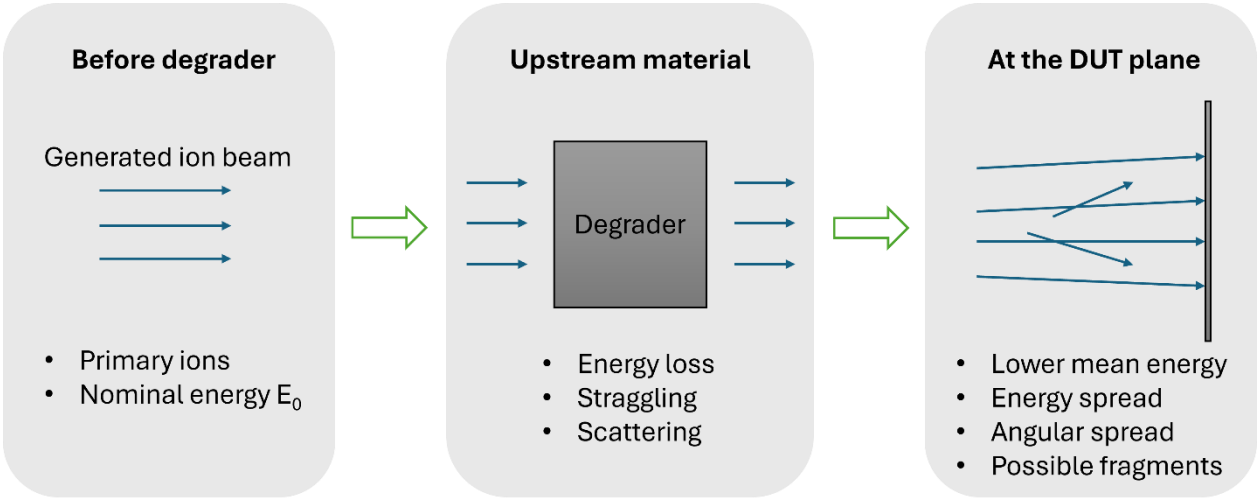

Figure 5: Schematic illustration of the effect of upstream materials on the particle field at the DUT. The crossed material does not simply reduce the nominal beam energy, but also broadens the energy distribution, increases angular spread, and may generate secondary fragments, so that the DUT is exposed to an effective particle field rather than to the nominal beam alone

Because energy loss is stochastic, a degrader does not simply "shift" the beam energy, but it intrinsically broadens the residual energy distribution (energy-loss straggling) and can increase

angular spread via multiple Coulomb scattering, so the DUT field is better described by distributions rather than nominal values [10].

In the context of deposited-energy measurements in silicon, these effects typically manifest as peak broadening and, in aperture/package geometries, as changes in the relative visibility of trajectory families due to acceptance and path-length variations [7].

Figure 6: Example of the PMMA degrader system used in the HEARTS@CERN campaign to generate additional effective-energy conditions upstream of the PIPS diode. Reproduced from [6].

Fragmentation can enter the picture in two different ways: it can occur as an unintended product of crossing materials (including degraders and other upstream layers), producing secondary fragments that contribute to the particle composition at the DUT and can populate additional structures or tails in deposited-energy spectra [13]. Second, fragmentation can be exploited intentionally in a dedicated fragmentation target to produce "fragmented" or "secondary" ion beams whose composition is then selected and transported by beam optics, a concept widely used in fragment-beam production [14].

This thesis focuses on the first case: degraders are treated as part of the upstream material budget used to tune the beam energy at the DUT, while fragmentation is considered as a possible contributor to the effective field (secondary fragments) rather than as an intentionally produced secondary beam.

2.4 Deposited-energy spectroscopy with silicon diodes (PIPS/PIN)

Silicon diodes operated under reverse bias provide a direct way to perform deposited-energy spectroscopy of charged-particle fields, because the signal amplitude is proportional to the energy deposited in the depleted silicon region [7].

In a PIPS (Passivated Implanted Planar Silicon) diode, the p-n junction is formed by ion implantation and the surface is passivated to improve stability and reduce surface leakage current [15].

When an ion traverses the depletion region, it loses energy mainly by ionization, generating electron–hole pairs at a rate of approximately one pair per 3.6 eV of deposited-energy in silicon.

The electric field across the depleted region collects the carriers by drift, producing a transient current that is processed by front-end electronics so that each event can be converted into a pulse-height value. In practice, the pulse-height information is accumulated into a histogram (counts vs pulse height), which is interpreted as a deposited-energy spectrum after calibration and appropriate digital filtering.

Digital MCAs implementing pulse-height analysis (PHA) and list-mode acquisition are commonly used for this task, since they can provide both energy (pulse height) and timing information and can build energy spectra directly at the software level [16].

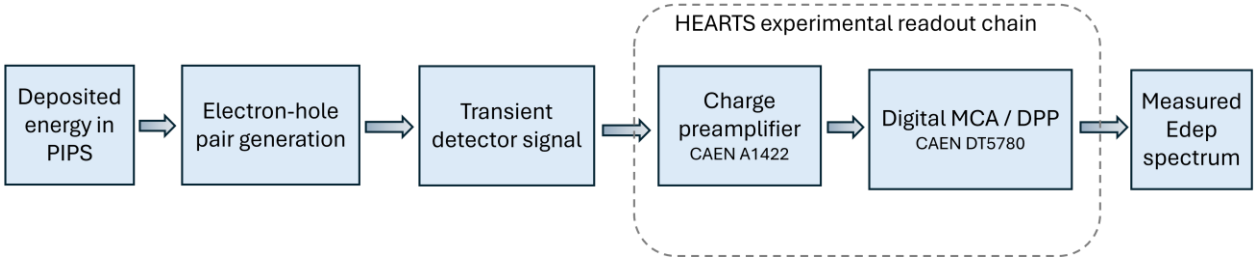

Figure 7: Measurement chain for deposited-energy spectroscopy with a PIPS diode in the HEARTS experimental setup.

This spectroscopy approach is particularly attractive for beam-quality checks because a single measured spectrum is sensitive to multiple aspects of the DUT field, including residual energy spread and the presence of additional energy-loss contributions upstream of the silicon [5].

A key point for VHE heavy-ion characterization is that realistic diode assemblies are not composed only by “bare silicon”: packages, entrance windows, housings, and apertures can define different trajectory classes with different crossed material thicknesses [7].

As observed in the HEARTS beam-quality measurements with PIPS diodes, these path differences, directly related to geometry, can produce distinct components (ex. “through-aperture” peak and a

"through-package" peak) and can evolve as degraders are introduced and the residual energy decreases.

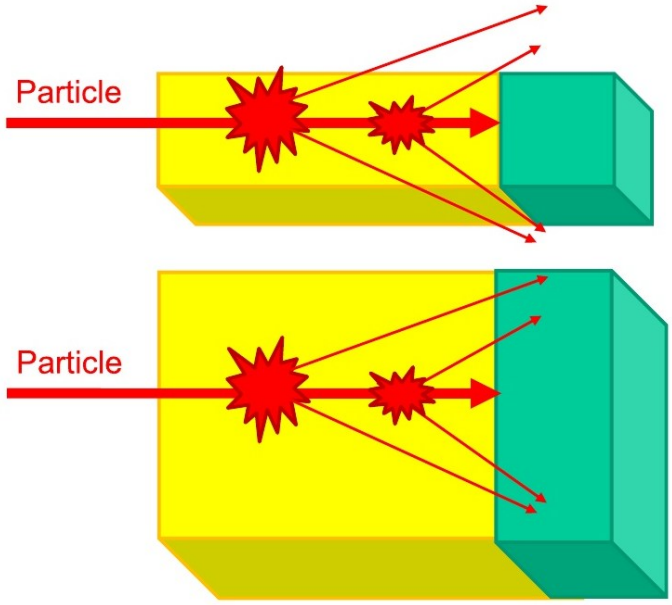

Figure 8: Conceptual sketch illustrating the effect of overlayers on energy deposition for different sensitive-volume sizes. Deposition enhancement associated with secondary electrons can be relevant for large sensitive volumes, such as PIPS diodes, while becoming less significant for very small sensitive volumes typical of advanced microelectronic devices. Reproduced from [11].

For this reason, deposited-energy spectra are powerful diagnostics, but their interpretation is not purely "by inspection" and typically benefits from transport simulations that include the relevant material stack and acceptance effects [7].

2.5 Simulation support: Monte Carlo and transient TCAD

In this work, two complementary simulation levels are used: (A) particle-transport Monte Carlo to model the radiation field and energy deposition in realistic geometries and (B) TCAD device simulations to model charge transport and transient signal formation in semiconductor structures. Monte Carlo transport codes simulate the passage of particles through matter by tracking interactions step-by-step in a user-defined geometry, enabling the prediction of quantities such as energy deposition, particle fluence, and secondary production under realistic material stacks. Geant4 is a widely used toolkit for this purpose, providing geometry and physics models needed to simulate particle transport in complex setups [17].

GRAS (Geant4 Radiation Analysis for Space) builds on Geant4 and provides a framework tailored to common radiation-analysis use cases, including charge deposit and SEE related quantities, which makes it convenient for beamline/detector studies [18].

In the context of the HEARTS beam-quality measurements, transport simulations are particularly valuable because the deposited-energy spectrum in a packaged diode can include multiple trajectory families (ex. through an aperture vs through additional package layers), whose relative contributions depend on geometry and scattering as well as on the residual beam energy [5] [7].

A practical example of what transport simulations provide in this thesis is the definition of an effective "energy at DUT" via a scoring plane placed immediately upstream of the detector, and the construction of a quantitative mapping between degrader thickness and residual mean energy (and energy spread) at the DUT.

This approach enables comparisons between measurements and simulations at equivalent DUT energies rather than relying exclusively on nominal settings, and it allows the incident-energy distribution (including straggling) to be propagated consistently into the predicted deposited-energy spectrum.

Transport simulations alone, however, do not directly explain how a given spatial ionization pattern turns into a measured transient current waveform, because that depends on the internal electric field, carrier mobilities, trapping/recombination, and the readout conditions of the device.

For this second layer of interpretation, TCAD device simulators (Synopsys Sentaurus Device) solve semiconductor transport equations in 2D/3D and explicitly support radiation-effects analyses, including single-event effects, by modeling charge generation and collection in a device structure [19].

In this thesis, TCAD transient simulations are used to model the time-domain current response of a PIN-like diode under an ionization condition parameterized by LET, enabling a direct comparison with measured transient waveforms and complementing the beam-level Monte Carlo picture.

Overall, the Monte Carlo and TCAD approaches address different questions: Monte Carlo links beamline + materials + geometry to the distribution of energy deposition events, while TCAD links device physics to the corresponding transient electrical response.

Their combination is therefore well suited to the workflow adopted in the following chapters, where Chapter 3 and 4 focus on reproducing and interpreting deposited-energy spectra with Geant4/GRAS, and Chapter 5 focuses on transient signal formation with TCAD.

Chapter 3 – Geant4/GRAS simulation framework

3.1 Scope and datasets

This chapter presents Geant4/GRAS simulations developed in the context of the HEARTS beam-quality measurements and aimed at reproducing the measured deposited-energy spectra in a silicon PIPS diode. The analysis is organized into two simulation blocks, corresponding to the two experimental campaigns reported in the HEARTS framework: a CERN dataset with Pb-208 beams and a GSI dataset with U-238 beams [5].

The purpose of separating the study into two blocks is to enable a consistent comparison of spectral features across different facilities and beam conditions, while keeping the simulation strategy and detector model consistent throughout the chapter. The common detector-package geometry and its GDML implementation are described in Section 3.2, and the common simulation/analysis workflow (including the definition of the key scored quantities) is described in Section 3.3 [5]. Results are then presented separately for the CERN Pb-208 configurations and for the GSI U-238 configurations in the subsequent sections.

In the following, the lists of reference beam configurations analyzed in the HEARTS deliverable (used for direct comparison in Chapter 4) are reported for both facilities (CERN and GSI) along with the extended set of Geant4/GRAS simulations performed for the Pb-208 part. For traceability, configurations are listed together with the nominal facility settings reported in the HEARTS deliverable. For the no-degrader configurations, the reported beam energy corresponds directly to the facility “Energy at DUT”. For the degrader configurations, instead, the quoted beam energy identifies the reference beam condition before the additional degrader, while the residual energy at the DUT is reconstructed in the simulations as described in Section 3.3. In the Geant4/GRAS simulations, the primary ion source energy is therefore not generally taken equal to the nominal accelerator energy, because ions in the experimental setup may already lose part of their energy before reaching the degrader or the detector, whereas this initial transport section is not reproduced in the same way in the simulations. The source energy is accordingly adjusted so that the relevant scored energy matches the facility-reported reference value.

Reference CERN (Pb-208) configurations reported in HEARTS:

- Pb-208, 908 MeV/u, without degrader (Nominal energy = 1000 MeV/u)
- Pb-208, 387 MeV/u, without degrader (Nominal energy = 500 MeV/u)
- Pb-208, 387 MeV/u with PMMA degrader: 13.0 mm (Nominal energy = 500 MeV/u)
- Pb-208, 387 MeV/u with PMMA degrader: 16.5 mm (Nominal energy = 500 MeV/u)
- Pb-208, 387 MeV/u with PMMA degrader: 18.5 mm (Nominal energy = 500 MeV/u)
- Pb-208, 387 MeV/u with PMMA degrader: 19.5 mm (Nominal energy = 500 MeV/u)

In addition to the degrader thicknesses explicitly tested and reported in the HEARTS deliverable, extra PMMA thickness points were also simulated in order to better sample the transition regions (near discontinuities) and to support a more detailed sensitivity analysis and interpolation of the degrader-to-E_{DUT} relationship.

These additional PMMA thickness points simulated in this work (Pb-208, 387 MeV/u at DUT) are:

- 17.0 mm
- 17.5 mm
- 18.0 mm
- 19.0 mm
- 20.0 mm

Reference GSI (U-238) configurations reported in HEARTS:

- U-238, 883 MeV/u without degrader (Nominal energy = 900 MeV/u)
- U-238, 883 MeV/u with PE degrader 31.1875 mm (Nominal energy = 900 MeV/u)
- U-238, 169 MeV/u, without degrader (Nominal energy = 200 MeV/u)
- U-238, 141 MeV/u, without degrader (Nominal energy = 175 MeV/u)

3.2 Experimental setup and detector-package model

The experimental setup is reproduced in Geant4/GRAS by modelling a PIPS (Passivated Implanted Planar Silicon) silicon diode together with its package material. PIPS diodes are reverse-biased silicon diodes (as introduced in Section 2.4) in which the p-n junction is formed by ion implantation and the detector surface is passivated. This technology yields stable and reproducible junction

properties and helps reduce surface leakage currents, improving noise performance and long-term stability [15].

In the HEARTS campaigns considered in this work, the detector is a Mirion PIPS diode with 50 mm² active area and a 300 μm thick sensitive region (model FD50-14-300RM). The diode is operated at the manufacturer's recommended bias voltage (typically 60 V for the 300 μm thickness) to ensure efficient charge collection in the depleted region, and the detector capacitance is of the order of a few tens of pF. In practice, the measured signal is proportional to the energy deposited by the ion within the depleted silicon volume, which generates electron-hole pairs that are collected by drift in the electric field under reverse bias.

Compared with older silicon surface-barrier and diffused-junction detectors, Mirion's PIPS technology is designed to provide buried junction edges (avoiding epoxy edge sealing), thin and robust entrance windows, and significantly reduced leakage current, supporting stable spectroscopy operation. These features motivate the use of a PIPS diode as a robust spectroscopic sensor for heavy-ion beam characterization and provide the context for the detailed detector-package geometry model implemented in Geant4/GRAS and described next [15].

In the HEARTS methodology, beam quality is evaluated by measuring the deposited-energy spectrum in the active region of the PIPS diode. This observable is particularly suitable for very-high-energy heavy-ion beams because the deposited-energy is directly linked to the ion's energy loss in silicon and is therefore sensitive to both the incident beam conditions (ion species and residual energy at the detector) and to the effective material stack encountered before reaching the sensitive volume. Moreover, the detector package includes an aperture and surrounding housing layers, so different classes of trajectories (ions entering through the free aperture versus ions traversing additional package materials) can produce distinct components in the deposited-energy distribution. For these reasons, the simulations in this thesis focus on reproducing and interpreting the measured deposited-energy spectra, and a detailed Geant4/GRAS geometry model is required to correctly account for the detector stack and the associated path-dependent energy losses. The front side of the package features a circular aperture with radius 4 mm that partially exposes the central region of the silicon, while the peripheral part of the active area is covered by additional package layers. The figure below (Figure 9) shows a lateral and a semi-frontal view of the simulated detector, highlighting the stainless-steel housing, the elastomer layers, and the silicon active area [5] [7].

The same detector and beam-spot model are used for both simulation blocks (introduced in Section 3.1), so that changes in the spectral topology can be mainly attributed to the ion species, beam energy, and facility-dependent degrader settings rather than to differences in geometry.

The detector-package geometry is implemented in a dedicated GDML file and imported in Geant4/GRAS, with key dimensions defined through constants to ensure internal consistency and reproducibility across runs. The geometry is built as a set of coaxial cylindrical volumes aligned with the beam axis, and the sensitive silicon region is modelled as a 300 μm thick active volume with a radius of 6.5 mm.

In the GDML model, the package front wall ("HousingBottom") is represented as a stainless-steel ring of thickness 0.5 mm starting at the aperture radius, so that ions passing through the central hole do not cross the front steel, whereas other trajectories do. Immediately downstream, an elastomer layer (0.5 mm) made of Kapton Polyimide material and a polymer ring ("LBIPolymerBottom", 0.3 mm) made of Plexiglass material are included in front of the silicon, with the polymer also extending laterally ("LBIPolymerLateral", 1.7 mm). These elements are followed by the active silicon volume, a second elastomer layer (0.5 mm), and further subsequent components such as an aluminum "TransmissionContact" layer and additional polymer and steel structures (ex. "HousingWall" and "HousingTop"). This layered stack, combined with the aperture geometry, enables the coexistence of different trajectory families (aperture-dominated vs package-including paths) that can contribute to distinct components in the deposited-energy spectra.

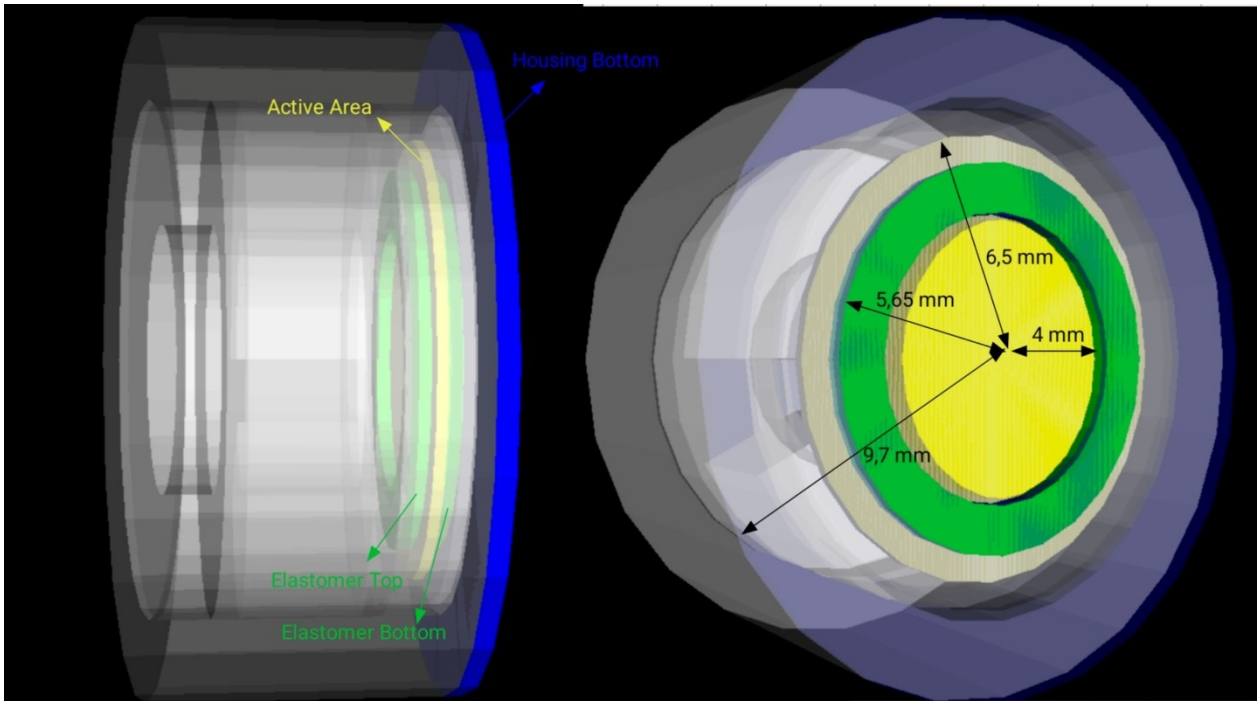

Figure 9: Lateral (left) and semi-frontal (right) views of the GDML-based detector model, showing the stainless-steel package, the front aperture (radius 4 mm), and the PIPS active silicon area (active radius 6.5 mm).

To complement the detector-package views shown in Figure 9, Figure 10 provides an overview of the transport geometry implemented in GRAS. This configuration will be discussed in more detail in the next section, where the simulation and scoring strategy are introduced.

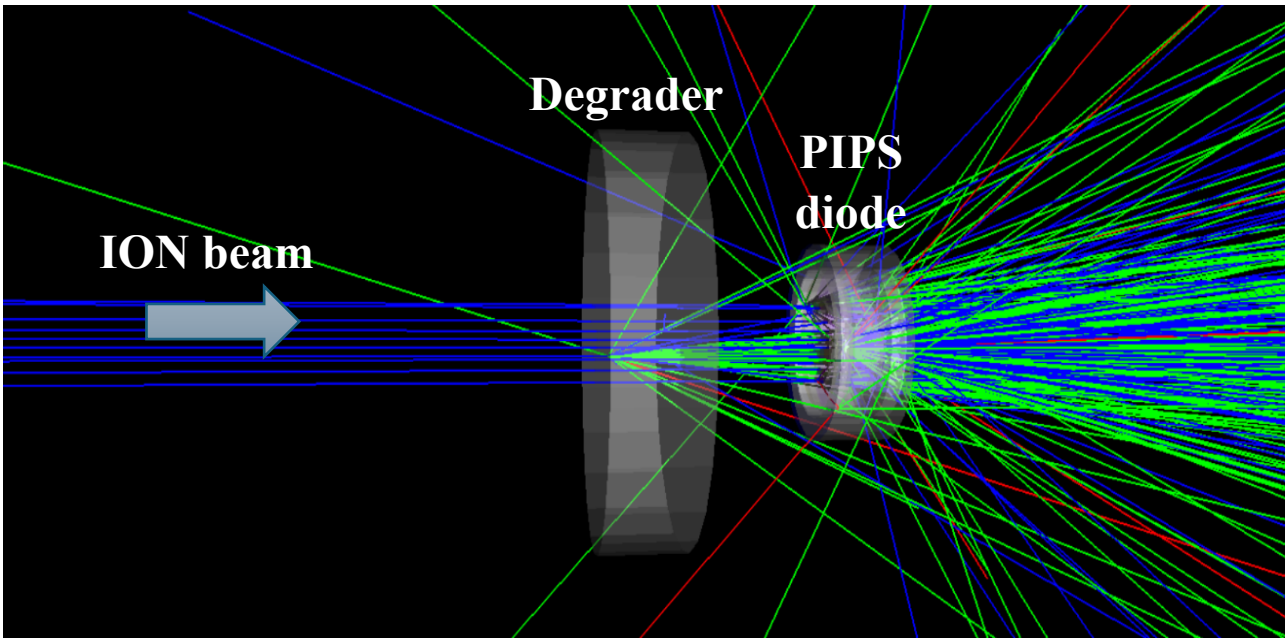

Figure 10: GRAS visualization of the beam-transport configuration used in this work, showing the primary beam crossing the degrader before reaching the packaged PIPS detector.

3.3 Simulation and scoring strategy

In this work, the beam energy 'at the DUT' is defined as the mean kinetic energy of primary ions at a reference point immediately upstream of the detector, identified in Geant4 by a specific "scoring volume" named ScoringPanelVolume in the GDML, which is a thin cylindrical disk (tube), implemented in GDML, placed at z = 10 mm along the beam axis. This volume has a radius of 20 mm and a thickness of 0.0001 mm which ensures that the scoring panel does not significantly perturb particle transport, while the proximity still allows the primary particle kinetic energy to be recorded immediately upstream of the detector.

For each event, the kinetic energy of the primary particle is recorded when it crosses the scoring plane. At the end of the run, the averages E_{kin} e E_{kin}/u (per nucleon) are computed only over the 'valid' events (those in which the primary crosses the scoring disk). Records are stored only for the primary ion. The value E_{kin} corresponds to the kinetic energy at the first crossing and events with no crossing are discarded (considered invalid).

In the HEARTS deliverable, the "Energy at DUT" is reported by the facility as a characteristic value of each tested beam configuration. In the simulations, the primary ion source energy is therefore adjusted so that the scored mean E_{kin}/u at the ScoringPanelVolume matches, as closely as possible, the corresponding facility-reported reference value. This is necessary because the initial transport section of the experimental setup, before the degrader or the detector, is not reproduced in exactly the same way in the simulations, so the nominal accelerator energy cannot be used directly as the simulation source energy. In the present dataset, the resulting simulated mean E_{kin}/uat the DUT is close to the facility-provided values (differences of only a few MeV/u), so residual discrepancies in deposited-energy spectra are interpreted mainly in terms of geometry/material stack and analysis sensitivities rather than a large mismatch in residual beam energy.The table below summarizes the data regarding the energy from the simulations and from experimental datasets. The following degrader thickness to E_{DUT} mapping, as well as the straggling statistics shown in the Section 3.5 are reported in detail only for the CERN Pb-208 (PMMA scan 0-20 mm), where a dense thickness grid is available. The GSI U-238 dataset includes only one PE-degrader configuration, therefore no analogous thickness-scan calibration curve is built.

PMMA thickness (mm)	Simulated $E_{sim} = E_{kin}/u$ (MeV/u)	E_{HEARTS} at DUT (MeV/u)	$\Delta E = E_{sim} - E_{HEARTS}$ (MeV/u)	Primary Ions / Total Ions generated
0.0	387	387	0	10000/10000
13.0	214	210	+4	7220/10000
16.5	154	153	+1	6587/10000
17	145	n/a	n/a	6557/10000
17.5	135	n/a	n/a	6454/10000
18	125	n/a	n/a	6456/10000
18.5	114	113	+1	6294/10000
19	102	n/a	n/a	6171/10000
19.5	90	88	+2	6135/10000
20	86	n/a	n/a	3911/10000

Table 1: Simulated mean kinetic energy per nucleon at the DUT (ScoringPanelVolume) as a function of PMMA degrader thickness. For the configurations reported in the HEARTS deliverable (0, 13, 16.5, 18.5, and 19.5 mm), the corresponding facility-provided "Energy at DUT" values are also listed for comparison [5]. "Primary Ions / Total Ions generated" indicates the fraction of primary ions that reach and cross the scoring plane.

The table also reports the difference $\Delta E = E_{sim} - E_{HEARTS}$ for the configurations where E_{HEARTS} is the facility-provided energy at DUT. In the present dataset, the observed differences are small (0 to +4 MeV/u, within a few percent) and are consistent with uncertainties in the effective degrader properties (density and thickness), and the fact that the simulation value is a mean computed only on ions that reach the scoring plane.

A calibration curve relating the PMMA degrader thickness to the simulated residual mean beam energy at the DUT was built using the E_{kin}/u values scored at the ScoringPanelVolume for all simulated thickness points. Since this relationship is monotonic, it was interpolated using a piecewise-linear model and inverted to obtain an "equivalent thickness" t_{eq} for any target DUT energy, enabling comparisons between measurements and simulations at equivalent beam energy rather than at the same nominal degrader thickness. For each run, E_{kin}/u is recorded event-by-event when the primary ion crosses the scoring plane, and summary values are computed only over the subset of valid events (events in which the primary reaches and crosses the scoring plane). This definition ensures that the reported DUT energy characterizes the beam that effectively arrives at the detector entrance, rather than the full set of generated primaries.

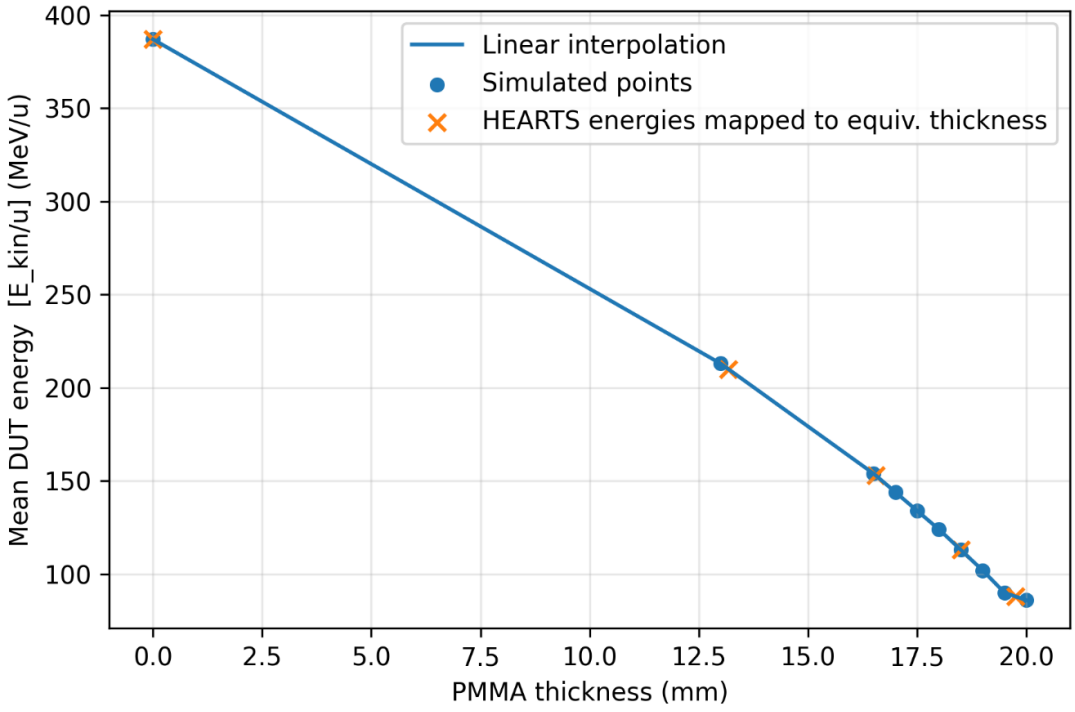

Figure 11: Calibration curve linking the PMMA degrader thickness to the simulated mean DUT energy E_{sim} (MeV/u), obtained from the ScoringPanelVolume for all simulated thickness points. The solid line represents a piecewise-linear interpolation of the simulated points, while the markers indicate the discrete simulation results. The facility-provided DUT energies are also shown after mapping to an equivalent thickness through inversion of the same interpolation.

For the configurations reported by the facility, the inverted mapping yields small offsets between nominal and equivalent thickness (for example 210 MeV/u corresponds to $t_{eq} = 13.18$ mm, and 88 MeV/u corresponds to $t_{eq} = 19.75$ mm in the present model). These offsets provide a quantitative way to interpret small discrepancies in "Energy at DUT" and to perform a more consistent comparison of deposited-energy spectra across experimental and simulated datasets.

At the end of each event, the deposited-energy value is written to a text file in CSV format and then analyzed as explained in Section 3.4, which then produces the histograms shown in the following [5].

3.4 Analysis workflow (histograms, normalization, peak extraction)

Post-processing is performed on the event-by-event deposited-energy (E_{dep}) in the active silicon region of the PIPS detector. For each simulated run, the quantity E_{dep} is recorded per event and

exported to CSV format, so that the deposited-energy spectrum can be interpreted as the statistical distribution of E_{dep} over the full set of simulated events.

Deposited-energy spectra are then built as histograms using a fixed bin width of 5 MeV, kept constant across configurations to enable a consistent comparison of peak positions and widths. Histogram bin centers are used as the x-axis representation for peak-search and fitting procedures. For shape comparisons, histograms are shown in normalized form (unit area), while for fit and parameter extraction the analysis is performed on raw bin counts. A logarithmic y-axis is used when needed to make small structures visible.

Peak positions are first estimated with an automatic peak-search on a smoothed version (smoothing is applied with a Gaussian filter with sigma = 1.2 bins) of the histogram and the peak-search is performed above a minimum energy threshold (50 MeV) to avoid the low-energy region. Also, a minimum separation between peaks is imposed to prevent counting the same structure twice.

To extract quantitative peak parameters, spectra are fitted with either one Gaussian, or two Gaussians depending on whether a second peak is found at sufficiently higher energy. The fit is performed using Poisson-like uncertainties per bin and returns peak centroids and widths, together with goodness-of-fit metrics such as χ^2/ndf. For each file, the fitted spectrum is saved as an image, and the extracted parameters are exported to a CSV table to enable plots and comparisons across configurations.

3.5 Degrader-to-E_{DUT} mapping and energy spread (Straggling metrics)

Energy-loss straggling refers to the statistical broadening of the residual-energy distribution of a charged-particle beam after it traverses an absorber (degrader). The nature of the energy-transfer processes leads to event by event fluctuation in the energy-loss, so that the energy at the DUT is more accurately described by a distribution rather than by its mean value only [10].

Even starting from an ideally monoenergetic beam, traversing a finite absorber thickness produces an intrinsic width in the residual-energy distribution, which tends to increase as the energy loss increases and may be accompanied by the development of a low-energy tail, particularly when the beam slows down significantly in the degrader [10].

In this thesis, the energy spread at the DUT is quantified robustly using percentiles of the E_{kin}/u distribution computed on valid events (those in which the primary ion crosses the scoring plane immediately upstream of the detector). In particular, $p50$ (the median) is reported as a measure of

central tendency, and $p16$ and $p84$ as the bounds of the central interval containing about 68% of the events. This choice makes it possible to describe the spread without assuming a priori a Gaussian shape for the distribution and reduces sensitivity to outliers and to tails that are not well sampled statistically.

PMMA thickness (mm)	$\sigma(E_{kin}/u)$ (MeV/u)	$p16$ (E_{kin}/u) (MeV/u)	$p50$ (E_{kin}/u) (MeV/u)	$p84$ (E_{kin}/u) (MeV/u)
0	0.000	387.00	387.00	387.00
13	0.611	212.97	213.57	214.17
16.5	0.814	153.33	154.13	154.94
17	0.843	143.78	144.60	145.47
17.5	0.882	133.88	134.75	135.68
18	0.922	123.55	124.48	125.41
18.5	0.997	112.76	113.78	114.69
19	1.032	101.39	102.41	103.40
19.5	1.121	89.25	90.39	91.46
20	3.174	83.41	87.56	89.20

Figure 12: Summary statistics of the residual kinetic energy per nucleon E_{kin}/u at the DUT as a function of PMMA degrader thickness. For each thickness, the table reports the standard deviation $\sigma(E_{kin}/u)$ and the percentiles $p16$, $p50$ (median), and $p84$, computed over valid events only (events in which the primary ion reaches and crosses the scoring plane immediately upstream of the detector).

Quantifying the spread upstream of the detector is useful to interpret the evolution of the energy-deposition spectra in silicon beyond a simple "shift" of the main peak: for a fixed detector geometry, an increase in the width of the incident-energy distribution is reflected in a broadening and/or greater complexity of the structures observed in the deposited-energy spectra. Moreover, because the statistics are computed only on valid events, the number n_{valid} reported together with the percentiles provides complementary information on the beam acceptance/transmission through the degrader, which becomes particularly relevant for larger thicknesses.

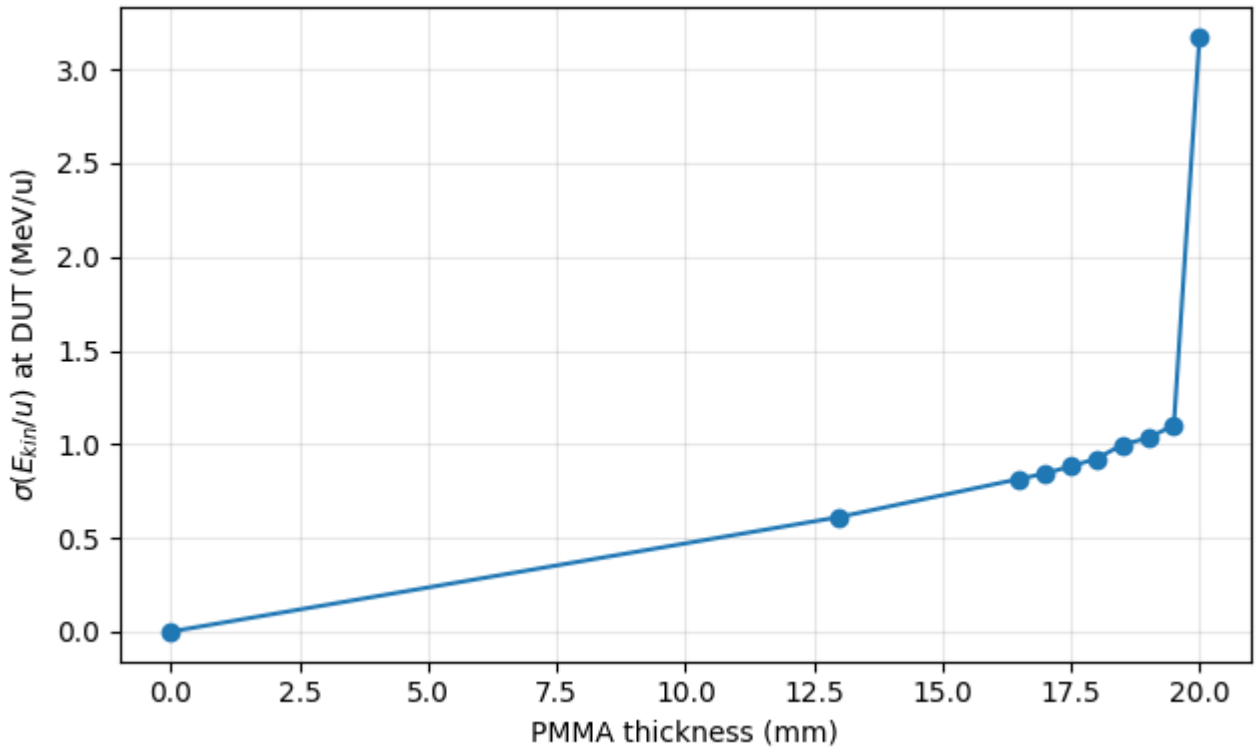

Figure 13: Standard deviation of the residual E_{kin}/u distribution at the DUT scoring plane versus PMMA degrader thickness (Pb-208, valid events only).

The figure above (Figure 13) shows the evolution of the DUT energy straggling with PMMA thickness, quantified here as $\sigma(E_{\mathrm{kin}}/u)$ which is the standard deviation of the event-by-event residual-energy distribution scored at the upstream scoring plane and computed over "valid events" only. As the degrader becomes thicker and the beam residual energy decreases, the spread generally increases due to the stochastic nature of energy-loss processes in the absorber, which broadens the residual-energy spectrum even for an initially monoenergetic beam. In the present dataset, $\sigma(E_{\mathrm{kin}}/u)$ grows gradually from intermediate thicknesses up to 19.5 mm and then exhibits a marked jump at 20 mm. This discontinuity can arise from a combination of a physical near-stopping regime, where small fluctuations in energy loss translate into large variations in the residual energy, and a selection effect due to the sharp reduction of the number of valid events at the largest thickness, which makes the residual-energy distribution conditional on "survivor" ions and therefore more sensitive to non-Gaussian tails and limited statistics. For this reason, the 20 mm point should be interpreted with caution and, if needed, complemented by inspecting the corresponding E_{kin}/u histogram (to check for a pronounced low-energy tail or outliers) and by reporting n_{valid} alongside σ and percentiles.

Chapter 4 – Geant4/GRAS results (CERN/ GSI)

4.1 Results: CERN Pb-208 deposited-energy spectra

The results in this chapter are presented as a function of the effective energy at the DUT, defined as the primary-ion kinetic energy per nucleon scored at the upstream scoring plane (ScoringPanelVolume).

The complete set of simulated configurations, including the full PMMA thickness scan (0-20 mm) and the corresponding E_{DUT} values, is reported in Chapter 3 together with the degrader-to-E_{DUT} analysis and the DUT energy-spread (straggling) characterization.

For each configuration, a dedicated Geant4 simulation was performed by keeping the PIPS detector geometry, package model, and beam profile fixed, while varying only the beam initial energy and the presence/thickness of the upstream degrader.

This section presents the deposited-energy spectra in the PIPS detector obtained with Geant4 for the configurations listed above, together with a qualitative comparison against the experimental results reported in the HEARTS deliverable [5].

Each figure shows the normalized histogram of the event-by-event deposited-energy in the 300 µm active silicon region, along with the positions of the main maxima (vertical dashed lines) estimated with an automatic peak search on the histogram. In most cases two dominant peaks are found, while an additional weaker structure can appear for some cases.

For each configuration, the spectrum is shown both on a linear scale and on a logarithmic scale where the logarithmic view is used systematically to highlight low-count structures and tails.

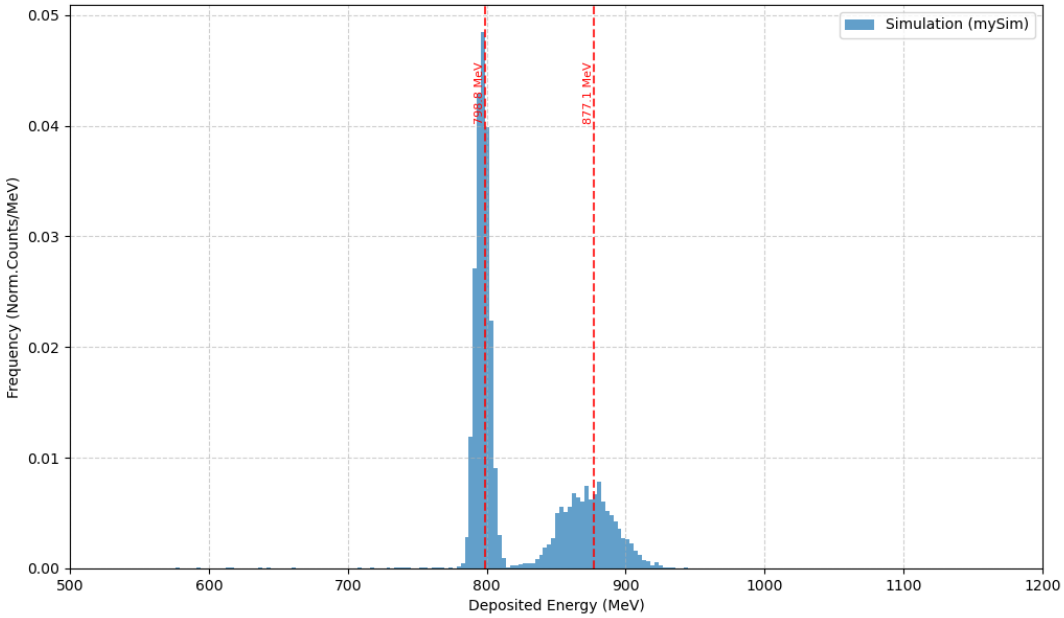

Figure 14: Pb-208, no degrader, E_{DUT}= 908MeV/u. Normalized deposited-energy spectrum E_{dep} in the 300 µm active silicon region of the PIPS detector for Pb-208.

For the Pb-208 configuration without degrader at $E_{\mathrm{DUT}} = 908$ MeV/u, the deposited-energy spectrum in the 300 µm active silicon region exhibits two well-resolved components (Figure 14), rather than a single peak. The linear-scale histogram highlights a narrow peak around 0.80 GeV and a broader structure centered at higher deposited-energy, around 0.87 GeV.

When shown on a logarithmic y-axis (Figure 15), the same spectrum emphasizes the low-count region at low deposited-energies and confirms that the two dominant components can be captured with a two-Gaussian model.

In this fit, the extracted centroids are $\mu_1 = 797$ MeV and $\mu_2 = 874$ MeV, with a much smaller width for the lower-energy "primary" peak than for the higher-energy one ($\sigma_1 = 5$ MeV vs $\sigma_2 = 19$ MeV).

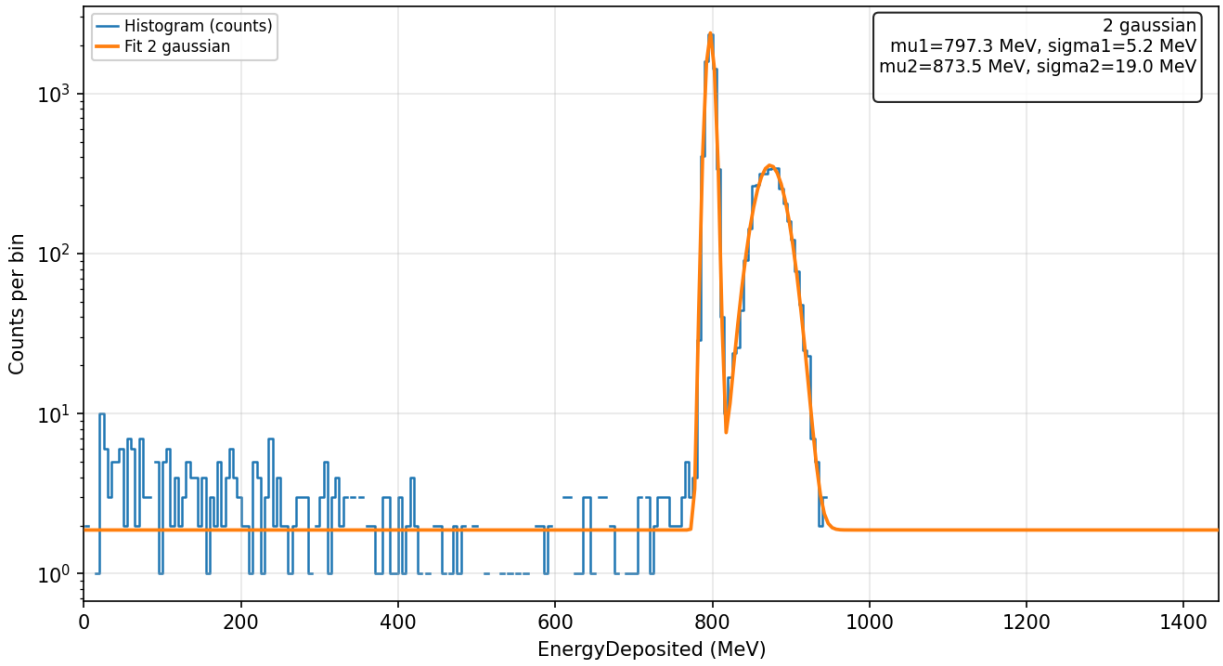

Figure 15: Pb-208, no degrader, E_{DUT}= 908MeV/u (log scale). Same spectrum shown on a logarithmic y-axis, with the overlaid two-Gaussian fit used to extract the peak positions and widths.

Within the geometrical interpretation adopted in this chapter, the presence of two main maxima is consistent with two trajectory families: ions entering predominantly through the front aperture ("hole" population) and ions that traverse additional package layers before reaching the sensitive silicon ("package" population). Even in the absence of a degrader, the additional upstream material budget outside the aperture is sufficient to produce a measurable separation in deposited-energy between these two populations at this beam energy.

In the HEARTS CERN campaign, the Pb-208 configuration with 1 GeV/u primary energy and no degrader (908 MeV/u at DUT) the corresponding peak positions reported are 672 MeV (primary peak) and 808 MeV (secondary peak), so the simulation reproduces the qualitative topology observed in HEARTS, but both peak locations are systematically shifted to higher deposited energies with respect to the experimental reference values [5]. As for the other CERN configurations, that we'll see below, this residual offset can be affected by differences in the effective material budget and in configuration set-up so the comparison is best interpreted primarily in terms of spectral morphology and relative peak structure rather than absolute calibration at this stage.

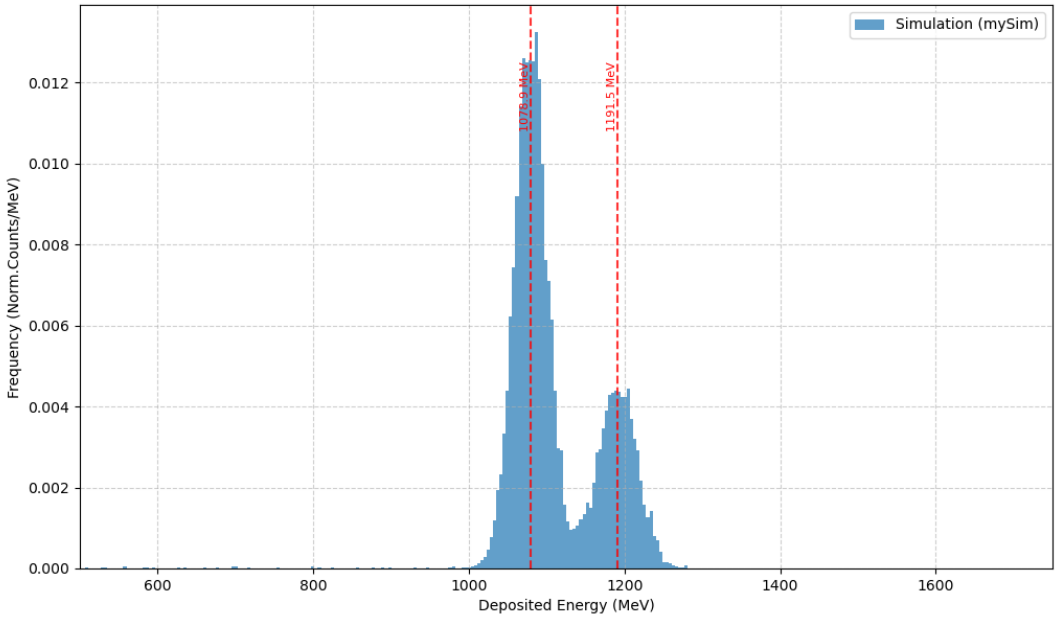

Figure 16: Pb-208, no degrader, E_{DUT}= 387MeV/u. Normalized deposited-energy spectrum E_{dep} in the 300 µm PIPS active silicon region for a Pb-208 beam.

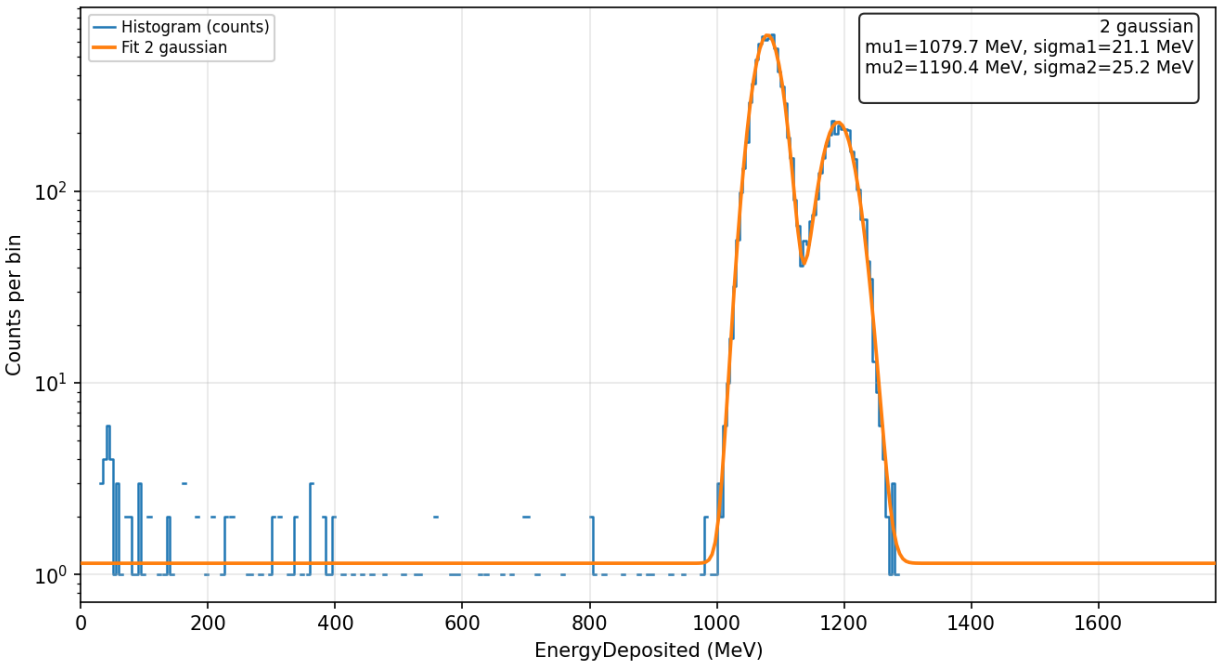

Figure 17: Pb-208, no degrader, E_{DUT}= 387MeV/u (log scale and fit). Same spectrum displayed with logarithmic y-axis, together with the two-Gaussian fit used to parameterize the two main spectral components.

The second simulated configuration is the one without degrader at $E_{\mathrm{DUT}} = 387$ MeV/u, for which the deposited-energy spectrum in the 300 µm PIPS active region still exhibits two clearly separated peaks, as seen in the linear scale (Figure 16).

In the HEARTS CERN campaign, the corresponding Pb-208 configuration (500 MeV/u primary energy, 387 MeV/u at DUT, no degrader), the deposited-energy values at the primary and secondary peaks are 983 MeV and 1168 MeV, respectively while in the present GRAS simulation at the same nominal DUT energy, the spectrum is bimodal, with fitted centroids around $\mu_1 = 1079$ MeV and $\mu_2 = 1190$ MeV [5].

Therefore, while the overall topology (two dominant components) agrees with HEARTS, the simulated peaks are shifted to higher deposited energies and show a smaller peak-to-peak separation than the experimental values reported in the deliverable.

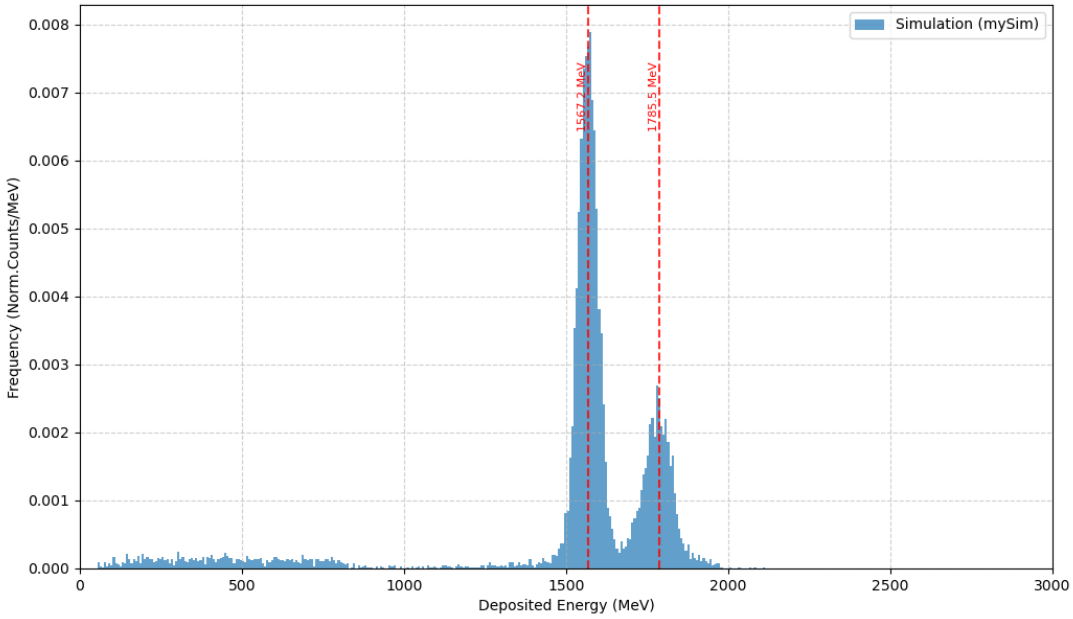

Figure 18: Pb-208, 13mm PMMA degrader, E_{DUT}= 214 MeV/u. Normalized deposited-energy spectrum E_{dep} in the 300 µm PIPS active silicon region.

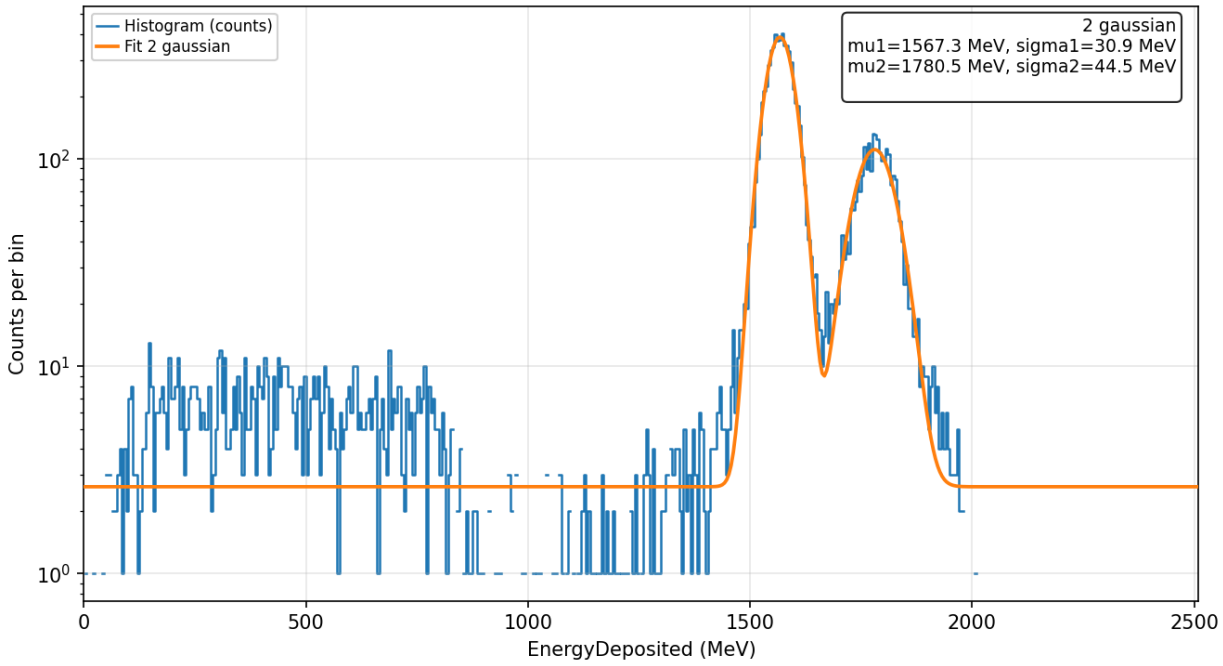

Figure 19: Pb-208, 13mm PMMA degrader, E_{DUT}= 214 MeV/u (log scale and fit). Same spectrum in logarithmic scale with the overlaid two-Gaussian fit used to parameterize the two main spectral components.

With a 13 mm PMMA degrader inserted upstream of the detector, the Pb-208 deposited-energy spectrum in the 300 µm active silicon region shows a more contrasted two-component structure, with a smaller minimum between the two maxima (Figure 18).

In the present run, the two-Gaussian fit returns peak centroids at $\mu_1 = 1567$ MeV and $\mu_2 = 1781$ MeV, with widths $\sigma_1 = 30.9$ MeV and $\sigma_2 = 44.5$ MeV (Figure 19).

The larger width of the two components with respect to the previous cases (indicated by the higher sigma) is due to a stronger event-by-event residual-energy spread of the generated ions, which is consistent with a larger path length for trajectories contributing to both peaks.

Compared to the no-degrader case, the spectrum is, as expected, also globally shifted to higher deposited energies, in line with the lower residual beam energy and reflecting the higher stopping power in silicon.

For the 13 mm PMMA configuration, the HEARTS deliverable reports an energy at DUT of 210 MeV/u (Table 1) and shows the corresponding deposited-energy spectrum in Fig. 5, again characterized by two peaks after re-binning and Gaussian fitting. The peak positions listed from the experimental dataset are 1459 MeV (primary peak) and 1987 MeV (secondary peak) [5].

Quantitatively, the first peak is higher in simulation, while the second peak is substantially lower than the HEARTS secondary peak, indicating that the model reproduces the bimodality but not the experimental relative spacing/ordering of the high-energy component for this setting.

Notably, the simulated mean DUT energy for 13 mm (215 MeV/u) is close to the HEARTS value (210 MeV/u), so the remaining mismatch is more likely driven by geometry/material-stack and analysis-procedure sensitivities than by an inconsistency in the nominal residual energy at the detector entrance.

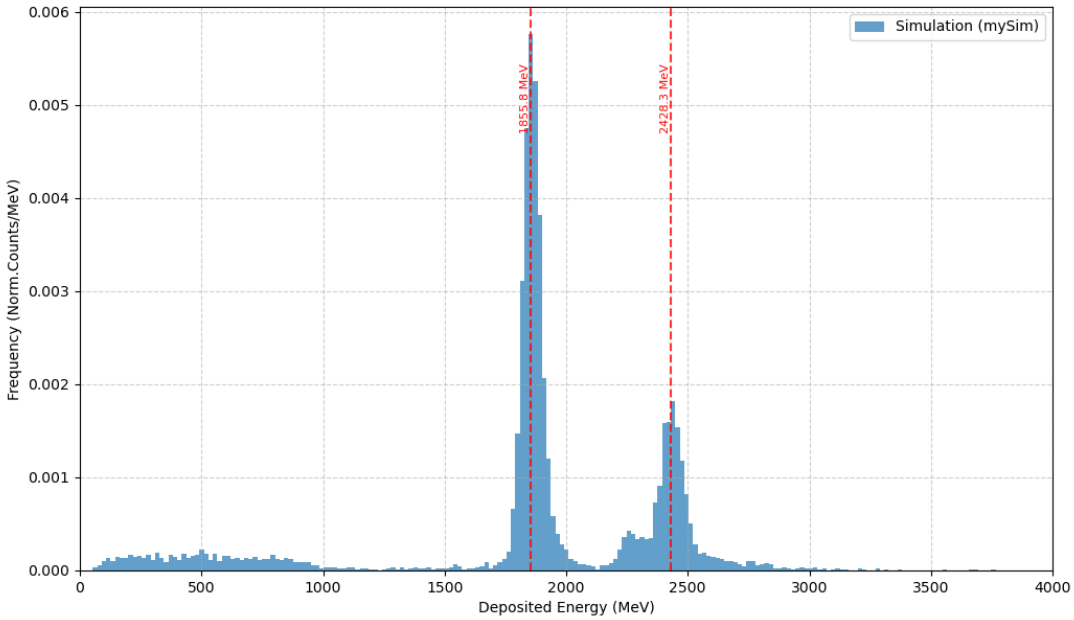

Figure 20: Pb-208, 16.5 mm PMMA degrader, E_{DUT} = 154 MeV/u. Normalized deposited-energy spectrum E_{dep} in the 300 µm PIPS active silicon region.

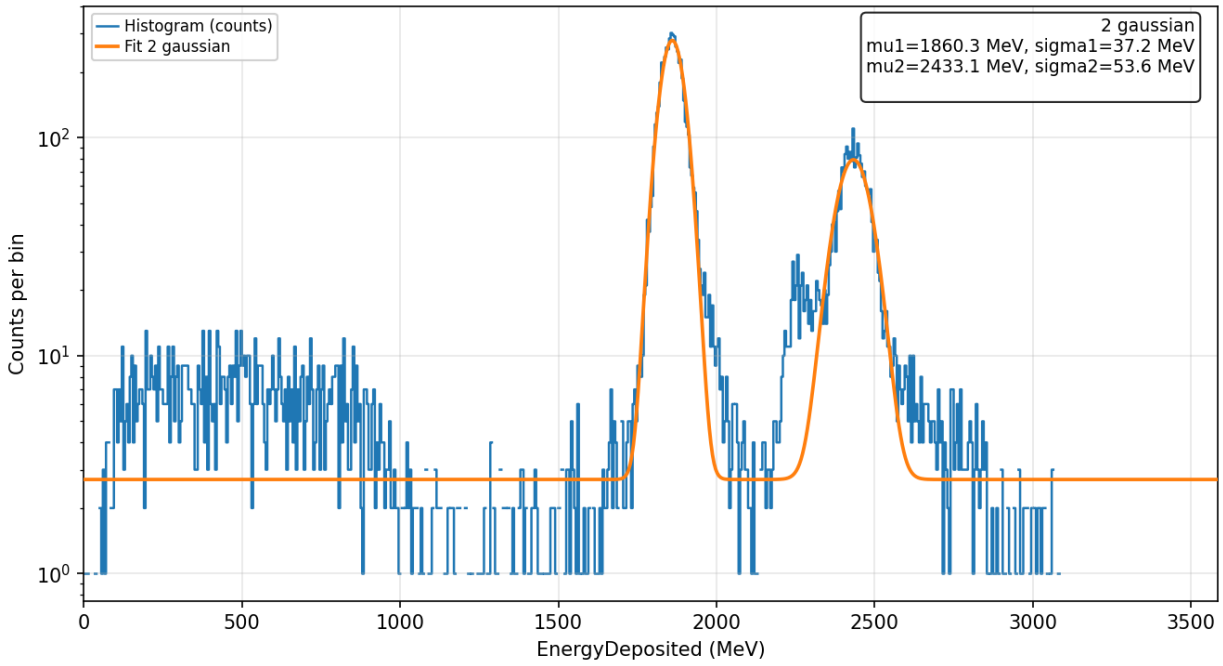

Figure 21: Pb-208, 16.5mm PMMA degrader, E_{DUT} = 154 MeV/u (log scale and fit). Same spectrum in logarithmic scale with the overlaid two-Gaussian fit used to parameterize the two main spectral components.

With a 16.5 mm PMMA degrader (corresponding to $E_{\mathrm{DUT}} = 153$ MeV/u in the HEARTS CERN configurations), the simulated Pb-208 deposited-energy spectrum in the 300 µm PIPS active silicon region remains dominated by two well-separated components.

A two-Gaussian fit yields $\mu_1 = 1860$ MeV with $\sigma_1 = 38$ MeV for the lower-energy peak and $\mu_2 = 2431$ MeV with $\sigma_2 = 59$ MeV for the higher-energy component, the latter being broader, consistent with a larger variability of trajectories sampling additional package material at reduced residual ion energy. In addition, a weak intermediate bump is starting to appear between the two dominant peaks. From a geometrical standpoint, this can be explained by a third, minority upstream material budget enabled by the mismatch between the inner radii of HousingBottom and ElastomerBottom (4.0 mm vs 4.2 mm), which creates a steel-only annulus in the 4.0–4.2 mm region.

Assuming a uniform beam spot of radius $R = 5$ mm, this annulus represents about 6.56% of the illuminated area, making it plausible for the associated population to appear as a resolvable intermediate feature at this reduced DUT energy.

In the HEARTS deliverable, the 16.5 mm PMMA configuration is summarized as a two-peak spectrum, and it reports only the primary and secondary peak positions (1936 MeV and 2428 MeV), with no additional intermediate component explicitly identified in the experimental analysis [5].

The simulation therefore reproduces the overall two-peak topology and provides a good agreement for the secondary peak position (~2432 MeV vs 2428 MeV), while the primary peak is shifted to lower deposited energies (~1860 MeV vs 1936 MeV). The additional weak structure observed in simulation is interpreted as a geometry-driven subdivision of trajectories near the aperture edge that is not captured by the two-peak fit model adopted in the deliverable.

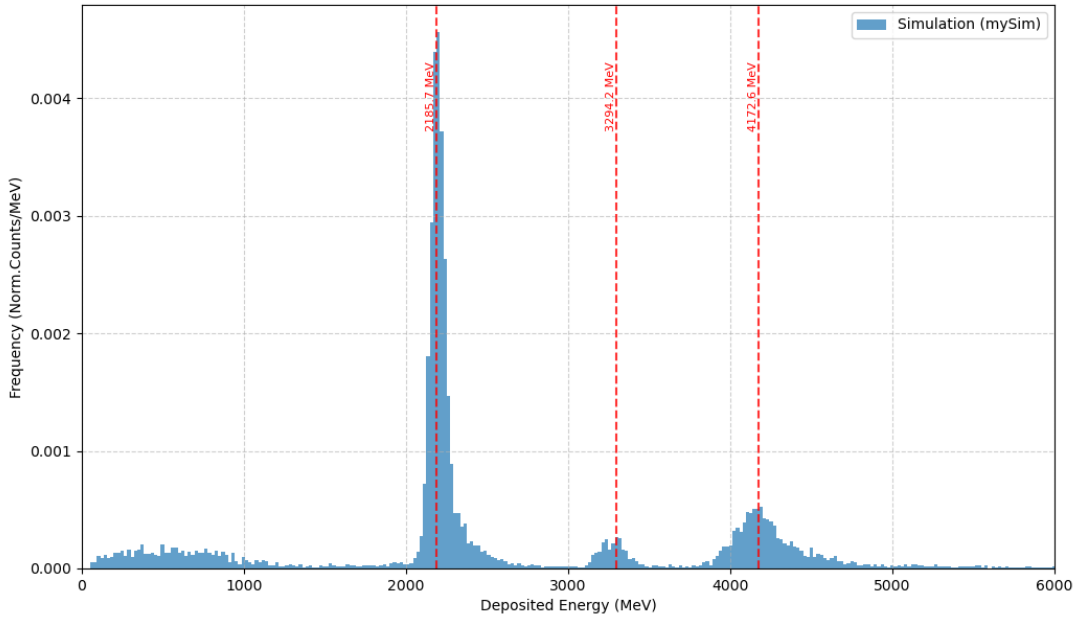

Figure 22: Pb-208, 18.5mm PMMA degrader, E_{DUT} = 114 MeV/u. Normalized deposited-energy spectrum E_{DEP} in the 300 µm PIPS.

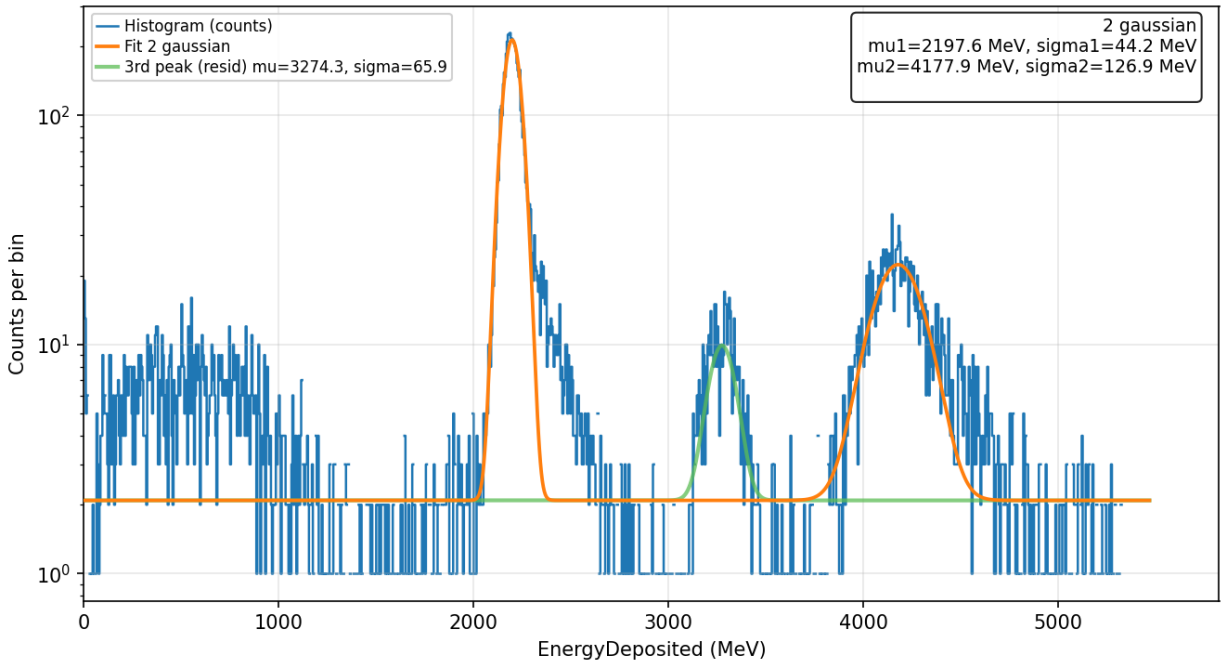

Figure 23: Pb-208, 18.5 mm PMMA degrader, E_{DUT} = 114 MeV/u (log scale and fit). Same spectrum in logarithmic scale with the overlaid two-Gaussian fit used to parameterize the two main spectral components.

With an 18.5 mm PMMA degrader, the simulated deposited-energy spectrum still shows two main components, but the overall shape differs from the thinner-degrader cases. Two-Gaussian fit yields $\mu_1 = 2197$ MeV and $\sigma_1 = 44$ MeV for the first peak and $\mu_2 = 4177$ MeV and $\sigma_2 = 127$ MeV for the second peak, as in the previous cases, with a much broader second component. In this regime, the separation between the "aperture" and "package" populations becomes even more sensitive to event-by-event variations in path length and energy loss, and it can manifest as additional events between the two maxima (as we can see from the well resolved third component at $\mu_3 = 3274$ MeV between the two maxima) but also at smaller energies.

In the HEARTS report, for the thickest degraders (the present one of 18.5 mm degrader and the following one of 19.5 mm) the second peak is described as no longer clearly recognizable and an additional structure at lower deposited-energy is noted. For the PMMA 18.5-mm configuration the experimental dataset reports a primary peak at 2390 MeV and a secondary peak at 2109 MeV, with the extracted secondary component lying below the primary in deposited-energy [5]. In contrast, the present simulation still retains a pronounced high-energy "package population" peak well above the first maximum (around 4.18 GeV), indicating a substantial mismatch in peak topology in this low-energy/high-degrader regime.

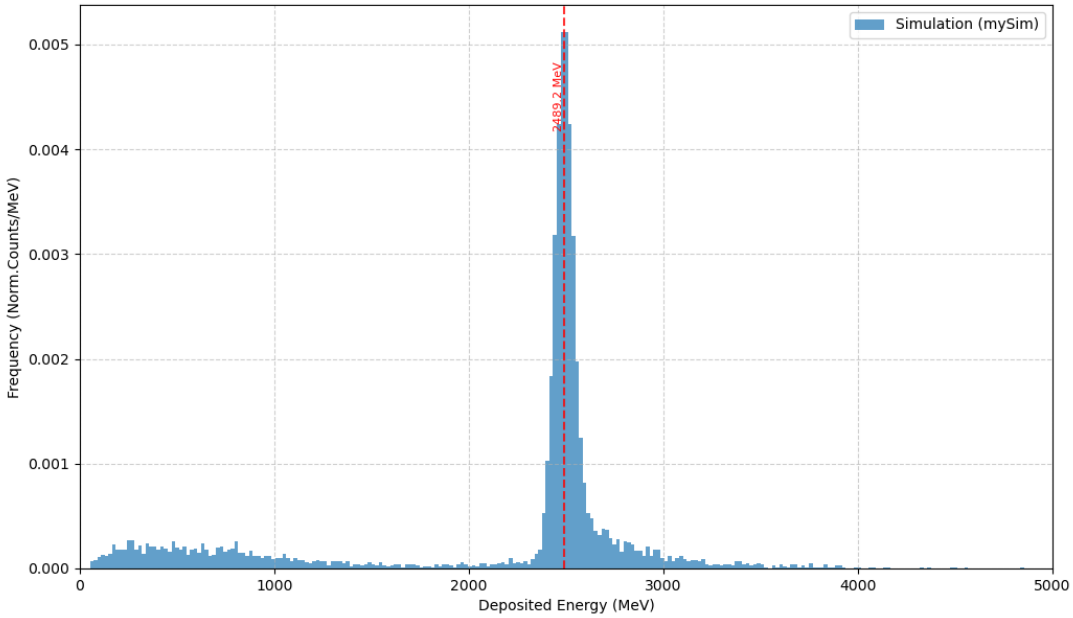

Figure 24: Pb-208, 19.5mm PMMA degrader, E_{DUT} = 90 MeV/u. Normalized deposited-energy spectrum E_{Dep} in the 300 µm PIPS.

In the final 19.5-mm PMMA degrader case, the simulated deposited-energy spectrum collapses into a single dominant peak, marking the first configuration in this Pb/PMMA scan where the "package" population no longer appears as a distinct high-energy component. A one-Gaussian fit of the main peak yields $\mu_1 = 2493$ MeV and $\sigma_1 = 49$ MeV. Track-by-track diagnostics confirm that, while both hole ($r < 4$ mm) and non-hole ($r > 4$ mm) ions trajectories can be observed at the upstream scoring plane, only the hole/aperture trajectories are consistently seen entering the active silicon volume, indicating that near the stopping regime the additional front materials associated with non-hole paths effectively suppress the contribution of "package" trajectories to the energy deposition in the 300-µm sensitive volume.

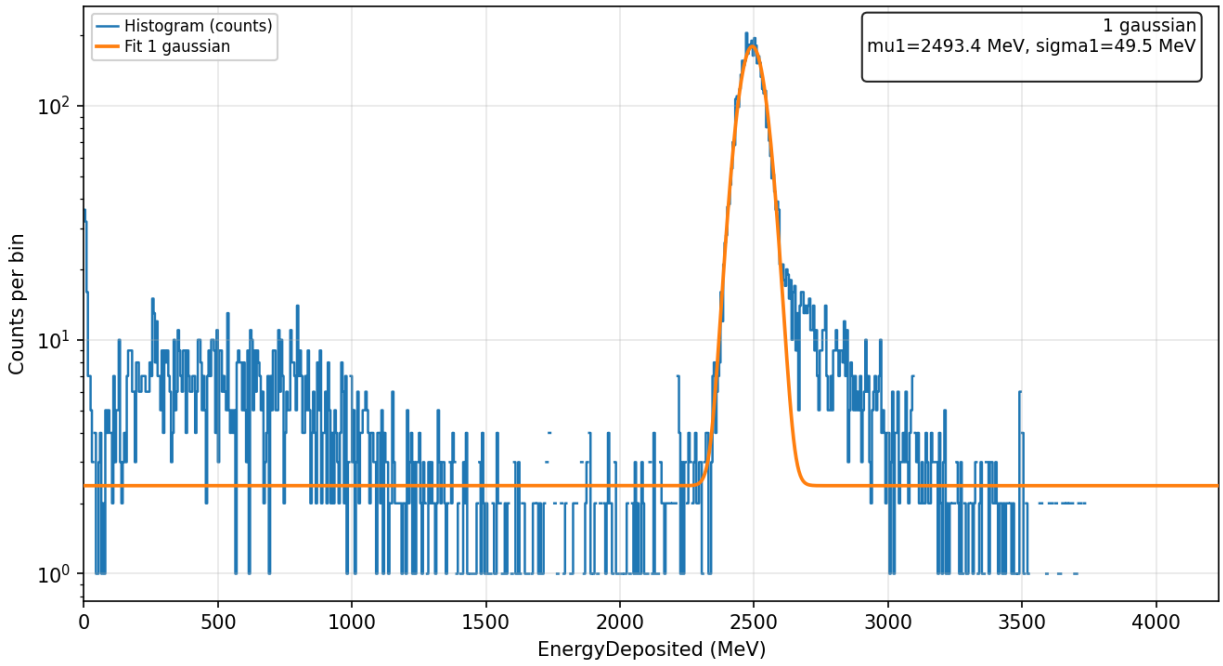

Figure 25: Pb-208, 19.5mm PMMA degrader, E_{DUT} = 90 MeV/u (log scale and fit). Same spectrum in logarithmic scale with the overlaid two-Gaussian fit used to parameterize the two main spectral components.

Even though HEARTS experimental dataset explicitly notes that, for the thickest degraders, the second peak at higher E_{DEP} is suppressed, an additional structure at lower deposited energies still appears. For this 19.5 mm PMMA configuration, a primary peak at 2843 MeV and a secondary peak at 2187 MeV are reported, showing a broader and more complex spectral shape than a simple single gaussian component [5]. Therefore, although the present simulation captures the qualitative trend of losing a clearly separable high-energy second peak at large degrader thickness, it still differs from the experimental spectrum morphology in this near-stopping configuration, suggesting that additional effects (ex. energy-loss tails, scattering/acceptance, or unmodelled upstream/downstream details) become dominant in the measured data.

A final quantitative comparison was performed for the CERN Pb-208 configurations by comparing the fitted GRAS peak positions with the experimental reference values reported in the HEARTS deliverable. For each configuration, the peak shift was defined as $\Delta E = E_{\mathrm{GRAS}} - E_{\mathrm{HEARTS}}$, and the corresponding relative deviation was computed as $\Delta E / E_{\mathrm{HEARTS}}$.

CERN Pb-208 configuration	HEARTS primary peak $\mu_{1,HEARTS}$ (MeV)	GRAS primary peak $\mu_{1,GRAS}$ (MeV)	$\Delta E_1 = \mu_{1,GRAS} - \mu_{1,HEARTS}$ (MeV)	$\Delta E_1/\mu_{1,GRAS}$ (%)
908 MeV/u, no degrader	672.0	797.3	+125.3	+18.6
387 MeV/u, no degrader	983.0	1079.7	+96.7	+9.8
214 MeV/u, 13 mm PMMA	1459.0	1567.3	+108.3	+7.42
154 MeV/u, 16.5 mm PMMA	1936.0	1860.3	-75.7	-3.91
125 MeV/u, 18.5 mm PMMA	2390.0	2197.6	-192.4	-8.05
90 MeV/u, 19.5 mm PMMA	2843.0	2493.4	-349.6	-12.30

Table 2: Comparison of the primary peak position in the CERN Pb-208 deposited-energy spectra between HEARTS reference values and Geant4/GRAS results. For each configuration, the table reports the peak centroid in deposited-energy (MeV), the absolute shift ΔE, and the relative deviation $\Delta E/E_{HEARTS}$ (%).

CERN Pb-208 configuration	HEARTS secondary peak $\mu_{2,HEARTS}$ (MeV)	GRAS secondary peak $\mu_{2,GRAS}$ (MeV)	$\Delta E_2 = \mu_{2,GRAS} - \mu_{2,HEARTS}$ (MeV)	$\Delta E_2/\mu_{2,GRAS}$ (%)
908 MeV/u, no degrader	808.0	873.5	+65.5	+8.11
387 MeV/u, no degrader	1168.0	1190.4	+22.4	+1.92
214 MeV/u, 13 mm PMMA	1987.0	1780.5	-206.5	-10.39
154 MeV/u, 16.5 mm PMMA	2428.0	2433.1	+5.1	+0.21
125 MeV/u, 18.5 mm PMMA	2109.0	4177.9	n.a.	n.a.
90 MeV/u, 19.5 mm PMMA	2187.0	n.a.	n.a.	n.a.

Table 3: Comparison of the secondary peak position in the CERN Pb-208 deposited-energy spectra between HEARTS reference values and Geant4/GRAS. “n.a.” indicates cases in which the spectral topology is no longer directly comparable or the secondary component is not resolved as a distinct peak in the simulation.

For the secondary peak, the comparison remains meaningful only up to the 16.5 mm PMMA case, where the spectrum still has a two-component structure. In this range, the agreement is best for the 387 MeV/u no-degrader and 154 MeV/u configurations, while the 214 MeV/u case shows a more pronounced negative deviation of the higher-energy component. For the two lowest-energy

configurations (18.5 and 19.5 mm PMMA), a direct secondary-peak comparison is no longer present: the HEARTS spectra are reported as more complex and no longer consistent with a simple two-peak behavior, whereas the simulation either retains a very-high-energy component (18.5 mm) or collapses to a single dominant peak (19.5 mm). Therefore, this close-to near-stopping regime shows that the discrepancy cannot be described as a simple constant shift but varies with configuration and residual energy along the Pb/PMMA scan.

4.2 Results: GSI U-238 deposited-energy spectra

This section presents the deposited-energy spectra obtained in the PIPS active region for the U-238 configurations of the GSI dataset. As for the CERN Pb-208 case in Section 4.1, the simulated spectra are compared against the experimental peak positions and qualitative features reported in the HEARTS deliverable. The goal is to reproduce the deposited-energy spectra in the PIPS detector for a heavier ion (Z = 92) and at a different facility, thereby providing a simulation reference to interpret the measured deposited-energy spectra and to cross-check the beam-quality indicators discussed in the HEARTS deliverable [5].

The detector geometry, package structure, and beam profile are identical to those used in the Pb-ion simulations: the PIPS is a 300 μm thick silicon diode with an active radius of 6.5 mm, housed in a stainless-steel cylinder (0.5 mm front wall thickness) with a front aperture of radius 4 mm, and the beam is modeled as a uniform cylindrical profile of a 5 mm radius, centered on the PIPS aperture. This ensures that any differences in spectral topology with respect to the Pb-ion case can be attributed primarily to the ion species (higher Z and A for U-238 with respect to Pb-208), the beam energy, and the presence or absence of a degrader, rather than to changes in the detector or beamline geometry.

At GSI, the tested configurations employ either no degrader or a polyethylene (PE) disk degrader of thickness 31.1875 mm, placed upstream of the detector to reduce the beam energy. The PE degrader has a density of approximately 0.94 g/cm³ and is the standard material used at GSI Cave A for beam-energy adjustment in heavy-ion radiation effects testing.

As in the Pb-ion case, the beam energy at the DUT is defined as the mean kinetic energy of primary ions crossing the scoring plane (ScoringPanelVolume) immediately upstream of the detector entrance and is computed only over valid events (those primaries that reach and cross the scoring

disk). The LET values stated in the table are facility-provided reference values at the silicon surface, reported in the HEARTS deliverable for each tested beam configuration [5].

As in the previous section, in all the plots shown here, the horizontal axis reports the event-by-event deposited-energy (E_{dep}) in the active silicon region of the PIPS diode, expressed in MeV. Each simulated ion event contributes one value to the creation of the histograms below, and that value is obtained by summing the energy deposited in the active silicon volume over all tracking steps occurring inside that volume, so the spectrum represents the statistical distribution of E_{dep} over the full run of the correspondent simulation.

The vertical axis represents how often a given deposited-energy value occurs, the number of events (counts) per histogram bin. The histogram is still shown as normalized counts so that the area under the distribution is unity, enabling a shape comparison across configurations with different statistics.

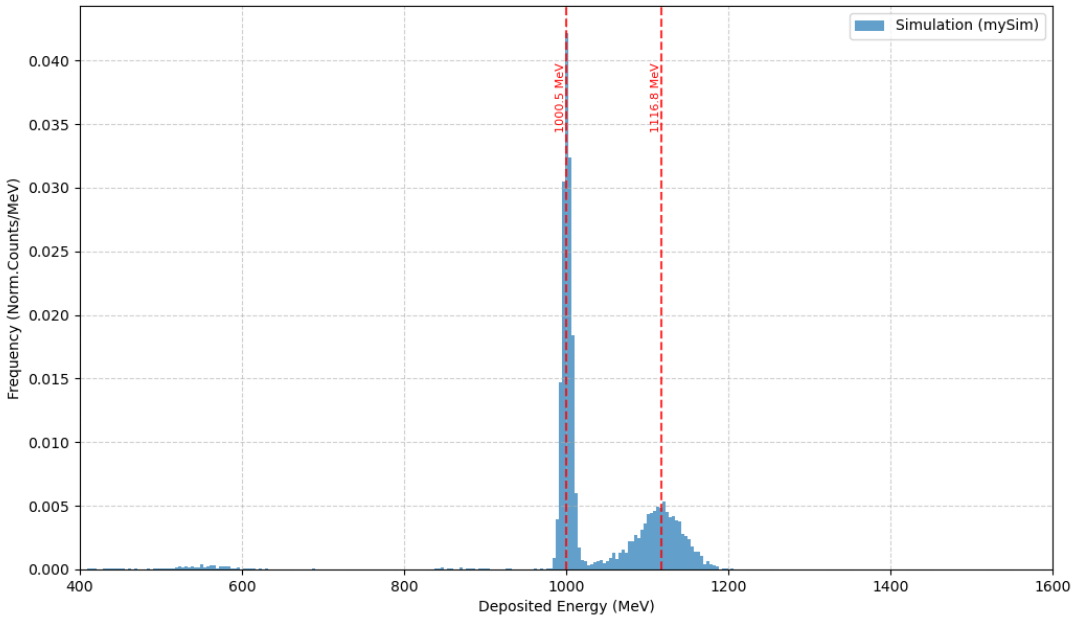

Figure 26: Uranium-238, no degrader, $E_{DUT} = 883$ MeV/u. Normalized deposited-energy spectrum scored event-by-event in the active region of the PIPS detector.

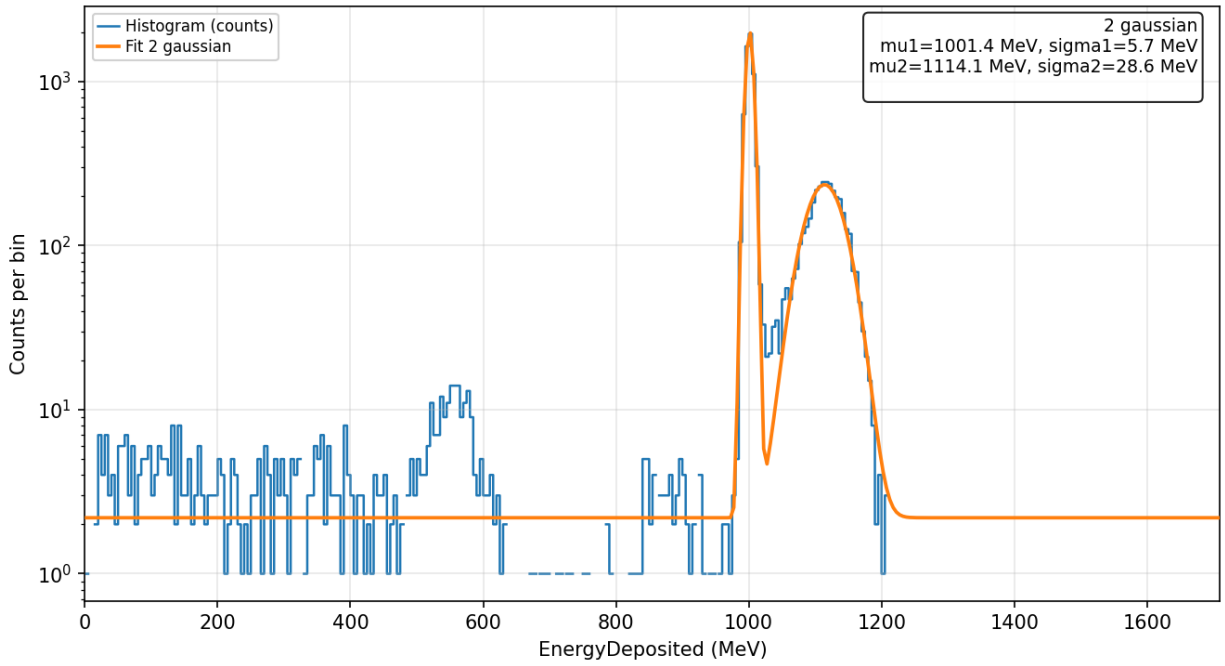

Figure 27: Uranium-238, no degrader, $E = 883$ MeV/u. Spectrum shown in logarithmic scale, with the overlaid Gaussian components used to model the main peaks with the corresponding fit parameters (μ, σ).

In the first simulation with U-238, and a generated beam of 883 MeV/u without additional degrader the deposited-energy distribution exhibits, consistently with the Pb-208 spectra discussed above, two well-defined dominant peaks. In this analysis, the two dominant components are modeled using the same two-Gaussian fit, yielding $\mu_1 = 1001$ MeV and $\sigma_1 = 5.7$ MeV for the left peak and $\mu_2 = 1114$ MeV and $\sigma_2 = 28.6$ MeV for the secondary peak.

As in the HEARTS interpretation for PIPS spectra, the presence of two main peaks is still consistent with the two trajectory families: ions entering through the front aperture ("aperture/hole" population) and ions reaching the sensitive silicon after traversing additional package materials ("package" population), as detailed in the stack in Section 3.2. In the HEARTS reference data for the same configuration, the reported peak positions are $\mu_1 = 852.0$ MeV and $\mu_2 = 1040.6$ MeV [5].

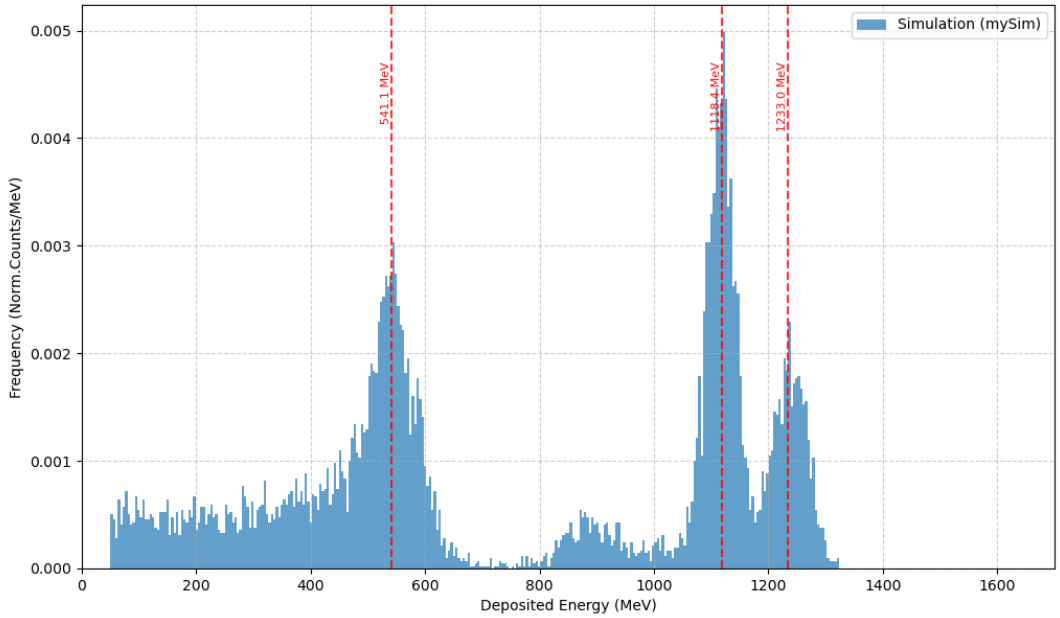

Figure 28: Uranium-238, PE degrader thickness 31.1875 mm, $E = 883$ MeV/u. Normalized deposited-energy spectrum scored event-by-event in the active region of the PIPS detector.

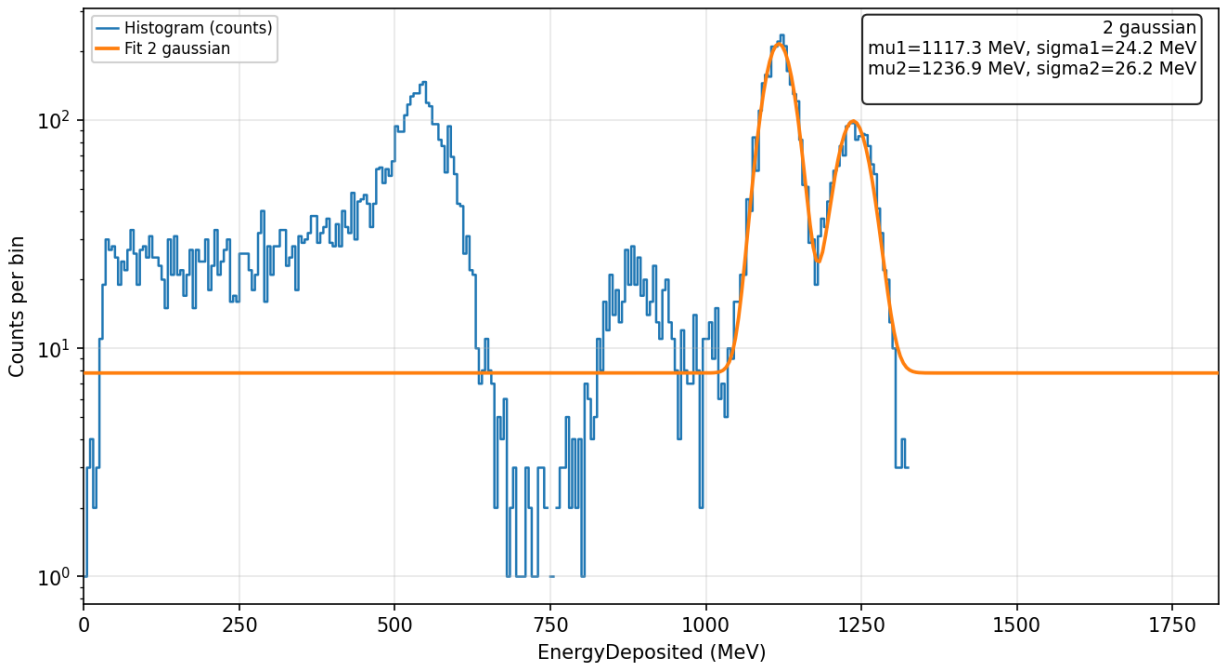

Figure 29: Uranium-238, PE degrader thickness 31.1875 mm, $E = 883$ MeV/u, $R = 5$ mm. Same spectrum shown in logarithmic scale, with the overlaid two-Gaussian fit of the main peaks and the corresponding fit parameters (μ,σ).

With the 31.1875-mm polyethylene (PE) degrader inserted upstream of the detector, the U-238 deposited-energy spectrum becomes significantly broader and more structured compared to the

no-degrader case, consistently with the introduction of energy-loss straggling and a wider event-by-event distribution of the residual beam energy at the detector entrance. In the simulated spectrum, a pronounced low-energy region emerges (including a broad bump/plateau at a few hundred MeV), while the high-energy part retains two distinct maxima that can still be modeled with a two-Gaussian fit.

For this configuration, the two-Gaussian fit applied to the two main high-energy components yields peak positions $\mu_1 = 1117$ MeV and $\sigma_1 = 24.2$ MeV for the left peak, and $\mu_2 = 1236$ MeV and $\sigma_2 = 26.2$ MeV for the right peak.

In the HEARTS deliverable, the corresponding GSI configuration (U-238, 900 MeV/u primary energy, 606 MeV/u at DUT, 31.1875 mm PE degrader) also shows two peaks in the re-binned and fitted spectrum, and Table 4 reports peak positions at 962.82 MeV (primary) and 1170.7 MeV (secondary). Therefore, the simulation reproduces the qualitative topology reported by HEARTS [5] (broader spectrum with two recognizable components), while quantitative differences remain in the peak locations and in the relative weight of the low-energy tail/plateau, which are particularly sensitive to degrader modeling (material density/thickness and upstream layers) and to acceptance effects.

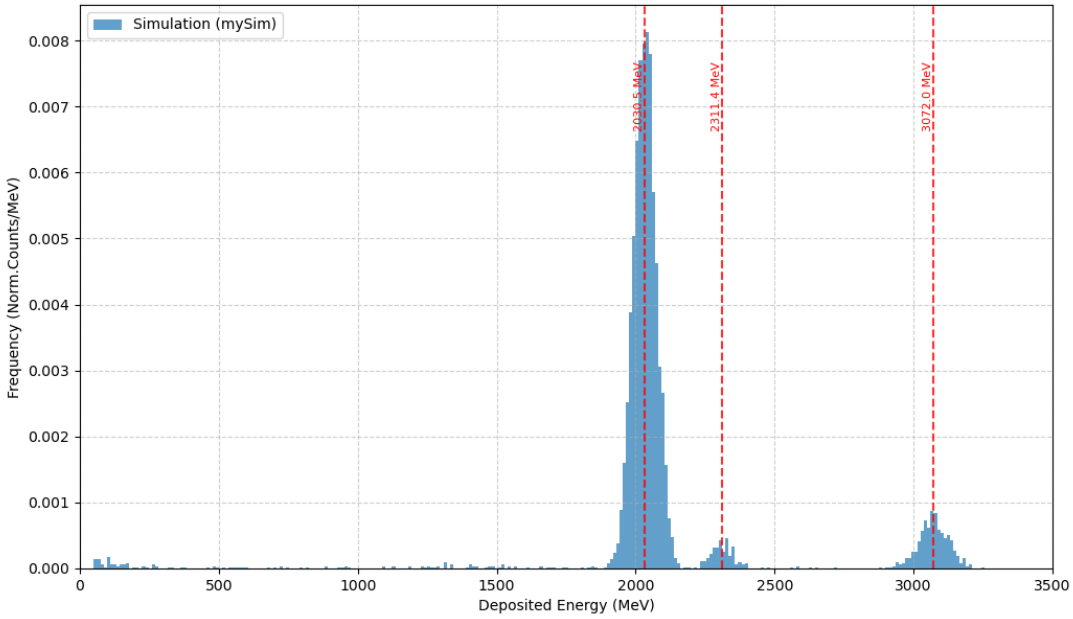

Figure 30: Uranium-238, no degrader, $E_{DUT} = 169$ MeV/u. Normalized deposited-energy spectrum scored event-by-event in the active region of the PIPS detector.

The last two simulated cases for the U-238 feature the lower generated energies with the first one being at $E_{DUT} = 169$ MeV/u without degrader (Figure 30), the deposited-energy spectrum is not significantly different from some of the other cases and still exhibits two clearly separated dominant components, together with a smaller intermediate structure between them. The two main peaks are described with a two-Gaussian fit, yielding $\mu_1 = 2033$ MeV and $\sigma_1 = 39.5$ MeV for the left peak and $\mu_2 = 3072$ MeV and $\sigma_2 = 44.0$ MeV for the right peak. In addition, an intermediate peak is visible around $\mu_3 = 2302$ MeV with $\sigma_3 = 38$ MeV.

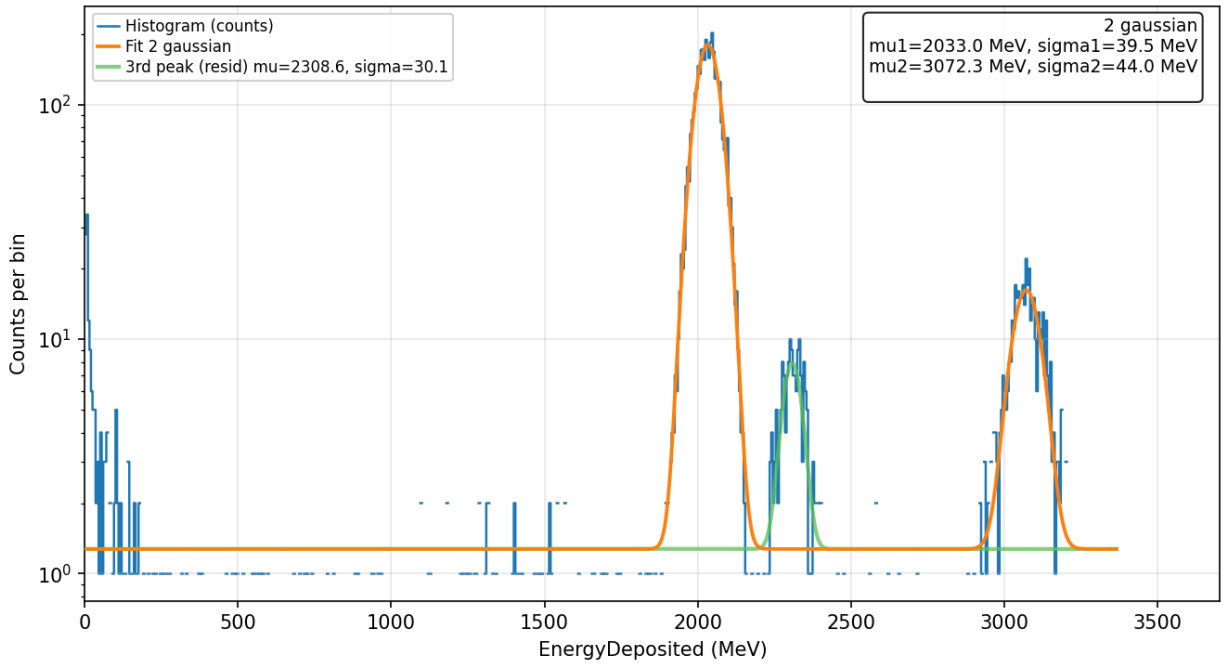

Figure 31: Uranium-238, no degrader, $E_{DUT} = 169$ MeV/u. Same spectrum shown in logarithmic scale, with the overlaid Gaussian components and the corresponding fit parameters (μ, σ); an additional intermediate peak is shown as a diagnostic overlay.

At this low DUT energy the separation between the two families becomes very large because the stopping power increases and path-length differences in the detector stack translate into sizeable differences in deposited-energy. The intermediate structure is treated as a minor population, associated with the geometry-driven subdivision of trajectories near the aperture edge in the current GDML model described previously for the lower energy cases analyzed for the Pb-208.

In the HEARTS deliverable, the corresponding GSI configuration is reported as “200 MeV/u primary energy, 169 MeV/u at DUT, no degrader” and Table 4 lists peak positions at 1907.0 MeV

(primary) and 2890.6 MeV (secondary) [5]. The simulation retains a multi-component structure, but the fitted peak positions are shifted to higher deposited energies and the separation between components is much larger than in the measurement, indicating that in this near-stopping regime the spectral morphology is especially sensitive to acceptance/scattering effects and to small differences in the effective material budget upstream and in the detector stack.

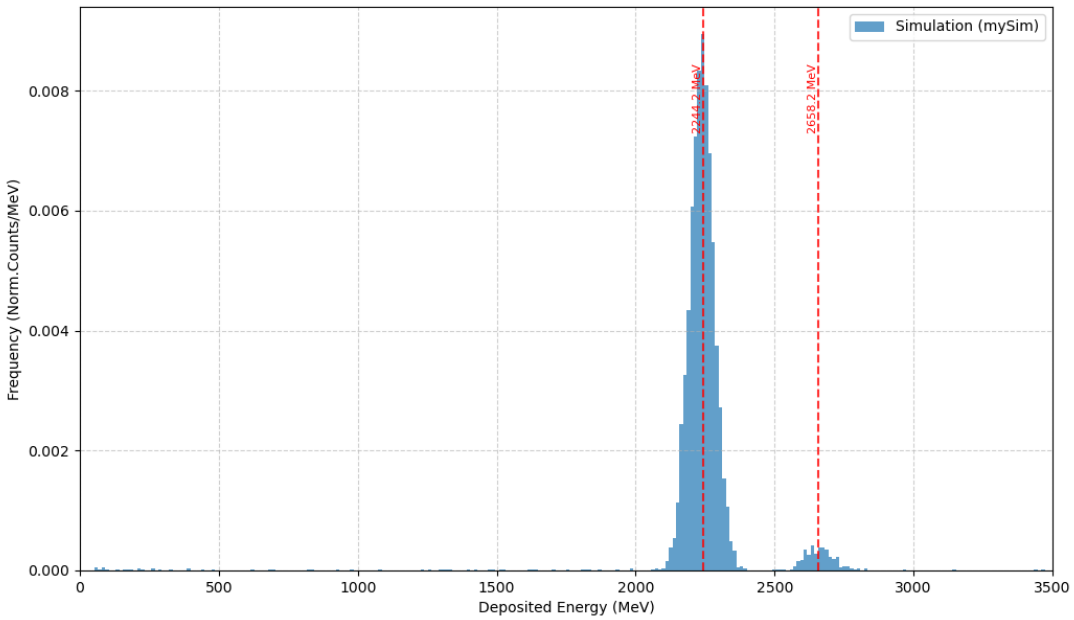

Figure 32: Uranium-238, no PE degrader, $E_{DUT} = 141$ MeV/u. Normalized deposited-energy spectrum scored event-by-event in the active region of the PIPS detector.

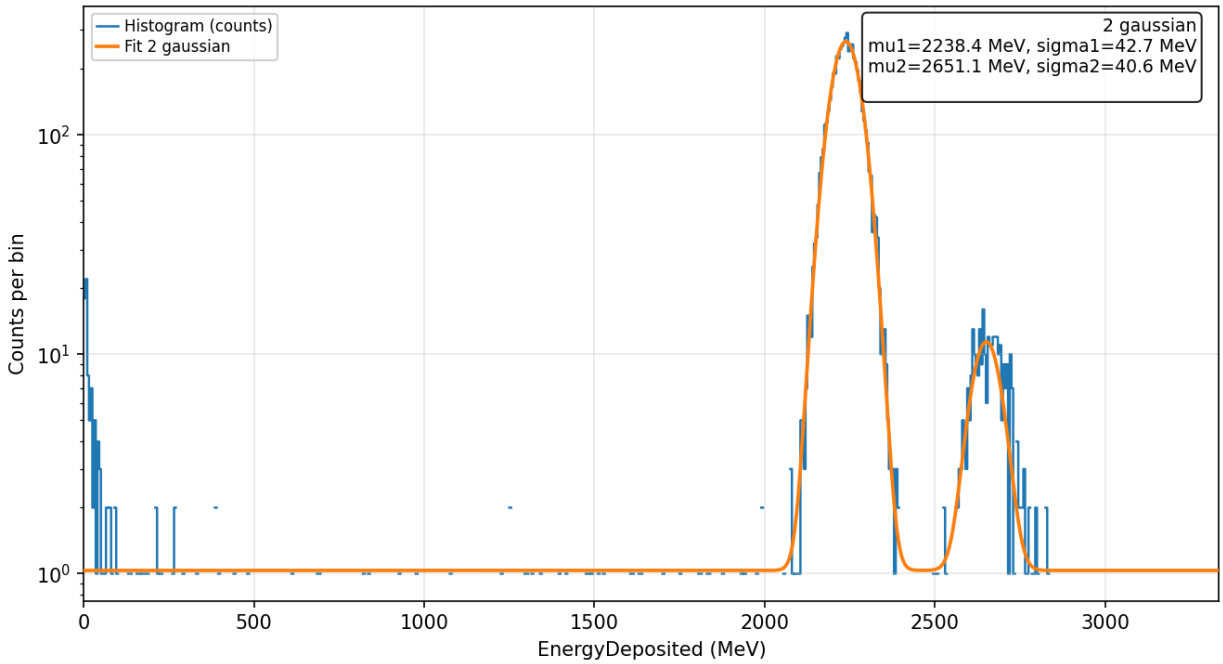

Figure 33: Uranium-238, no PE degrader, $E_{DUT} = 141$ MeV/u. Spectrum shown in logarithmic scale, with the overlaid two-Gaussian fit and the corresponding fit parameters (μ, σ).

For the U-238 configuration at $E_{DUT} = 141$ MeV/u without degrader, the deposited-energy spectrum in the 300-µm PIPS active silicon region exhibits two dominant components and no longer shows the intermediate structure observed at $E_{DUT} = 169$ MeV/u. The spectrum is modeled with the two-Gaussian fit, yielding $\mu_1 = 2238$ MeV and $\sigma_1 = 42$ MeV for the left peak and $\mu_2 = 2651$ MeV and $\sigma_2 = 40$ MeV for the right peak. Compared to the 169 MeV/u case, the disappearance of the additional component is consistent with the onset of a low-energy transmission/acceptance regime, where trajectory classes crossing a larger amount of package material become increasingly suppressed before reaching the sensitive region.

At such low DUT energy, the stopping power is significantly larger and even small differences in crossed thickness translate into large variations in residual energy and in the probability of surviving to the active volume, naturally leading to the progressive loss of the most material-intensive population (previously responsible for the highest-deposited-energy structure). This qualitative trend is in line with the HEARTS GSI analysis: for the "175 MeV/u primary, 141 MeV/u at DUT, no degrader" configuration, the deliverable reports a primary peak at 2152.21 MeV and does not provide a secondary peak value, indicating that the secondary population is not resolved/disappeared in the measurement [5].

In the present simulation, however, two peaks are still visible, and their positions are shifted to higher deposited energies with respect to the experimental values reported in HEARTS. This residual discrepancy suggests that, in this near-stopping regime, the measured spectrum is particularly sensitive to effects not explicitly included in the simplified upstream model (ex. additional material budget, scattering-driven acceptance losses, or a slightly different effective energy distribution at the detector entrance), which would further reduce the contribution of long-path package trajectories.

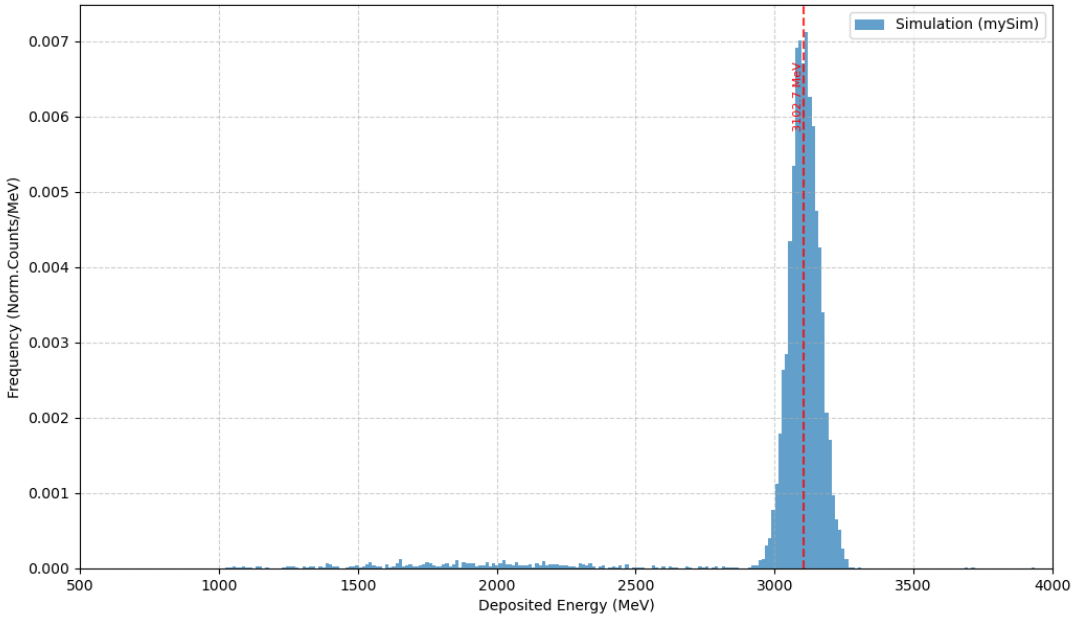

Figure 34: Uranium-238, no PE degrader, $E_{DUT} = 75$ MeV/u. Normalized deposited-energy spectrum scored event-by-event in the active region of the PIPS detector.

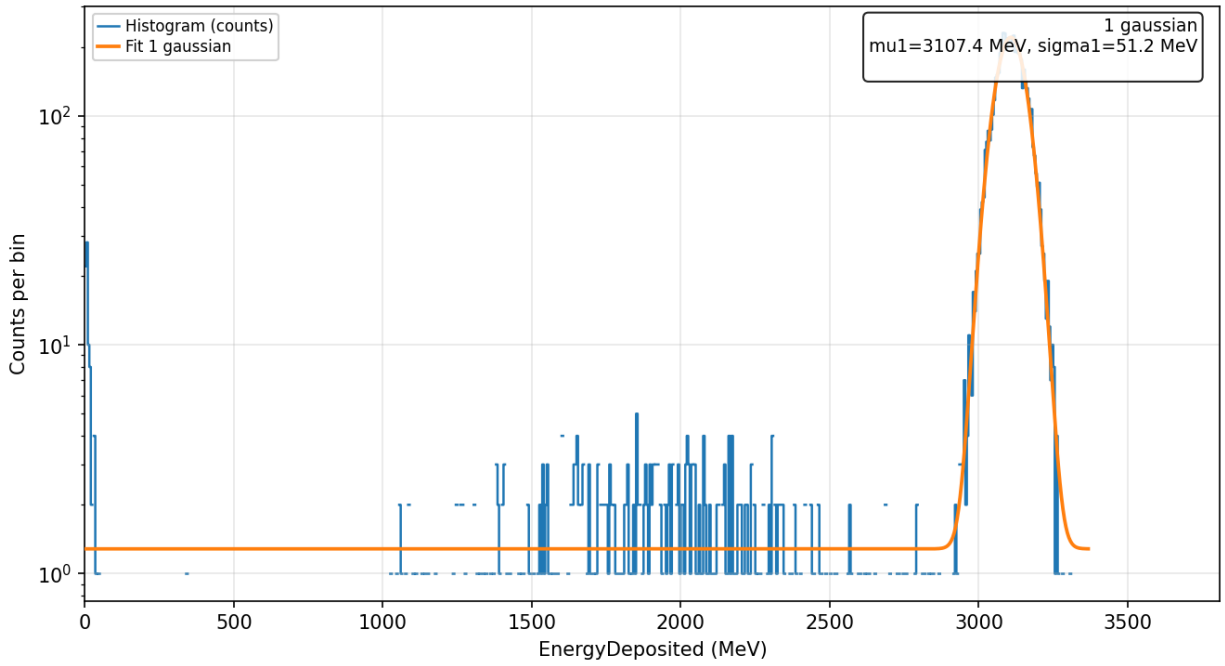

Figure 35: Uranium-238, no PE degrader, $E_{DUT} = 75$ MeV/u. Spectrum shown in logarithmic scale, with the overlaid two-Gaussian fit and the corresponding fit parameters (μ, σ).

The same summary comparison made for Pb-208 was also performed for U-238 by evaluating the difference between the simulated peak positions and the experimental reference values reported in the HEARTS deliverable.

For each configuration, the peak shifts were defined as $\Delta E_{\mathrm{Primary}} = \mu_1 - E_{\mathrm{dep,Primary}}$ and $\Delta E_{\mathrm{Secondary}} = \mu_1 - E_{\mathrm{dep,Secondary}}$. The corresponding relative deviations were computed as $\Delta / E_{\mathrm{HEARTS}}$.

The results, for the four configurations in HEARTS only, are reported in the following tables (Table 4 and Table 5).

GSI U-238 configuration	HEARTS primary peak $\mu_{1,HEARTS}$ (MeV)	GRAS primary peak $\mu_{1,GRAS}$ (MeV)	$\Delta E_1 = \mu_{1,GRAS} - \mu_{1,HEARTS}$ (MeV)	$\Delta E_1/\mu_{1,GRAS}$ (%)
883 MeV/u, no degrader	852.03	1001.36	+149.33	+17.53
883 MeV/u, with 31.1875 mm of PE degrader	962.82	1117.27	+154.45	+16.04

169 MeV/u, no degrader	1907.03	2033.01	+125.98	+6.61
141 MeV/u, no degrader	2152.21	2238.41	+86.20	+4.01

Table 4: Comparison of the primary peak position (μ_1) in the GSI U-238 deposited-energy spectra between HEARTS reference values and Geant4-GRAS results. For each configuration, the table reports the peak centroid in deposited-energy E_{dep} (MeV), the absolute shift ΔE, and the relative deviation $\Delta E/E$ (%).

A systematic positive shift of the GRAS peak positions with respect to the HEARTS reference values is shown, for all configurations where the comparison is available.

For the primary peak, the relative deviation decreases from about +16-17% at the highest energies (883 MeV/u, with and without degrader) to about +4-7% at the lowest energies (169 and 141 MeV/u), indicating that the mismatch is not a simple constant offset in deposited-energy.

GSI U-238 configuration	HEARTS secondary peak $\mu_{2,HEARTS}$ (MeV)	GRAS secondary peak $\mu_{2,GRAS}$ (MeV)	$\Delta E_2 = \mu_{2,GRAS} - \mu_{2,HEARTS}$ (MeV)	$\Delta E_2/\mu_{2,GRAS}$ (%)
883 MeV/u, no degrader	1040.60	1114.06	+73.46	+7.06
883 MeV/u, with 31.1875 mm of PE degrader	1170.70	1236.86	+66.16	+5.65
169 MeV/u, no degrader	2890.60	3072.31	+181.71	+6.29
141 MeV/u, no degrader	n.a.	n.a.	n.a.	n.a.

Table 5: Comparison of the secondary peak position (μ_2) in the GSI U-238 deposited-energy spectra between HEARTS reference values and Geant4-GRAS results. For each configuration where the secondary component is available, the table reports the peak centroid in deposited-energy (MeV), the absolute shift ΔE, and the relative deviation $\Delta E/E$(%). "n.a." indicates configurations where the secondary peak is not reported/resolved.

For the secondary peak, the deviations are of the order of +6-7% for the configurations where the secondary component is reported by HEARTS [5].

For the 141 MeV/u configuration, the secondary peak is not present anymore, so it is labeled as not available ("n.a."), and the last two quantities cannot be computed for that case.

The trend shown suggests that the residual discrepancy is dominated by effects that impact the absolute deposited-energy scale and may vary with beam energy and degrader conditions.

Possible causing factors include differences in the effective upstream material budget, energy-loss straggling modelling, and configuration-dependent acceptance losses, all of which can bias the peak locations extracted from the deposited-energy spectra.

In addition, the experimental peak positions reported in the deliverable are obtained after re-binning and Gaussian fitting, while the simulation peak positions are extracted from a fit performed on the simulated spectra.

Overall, the tables above (Table 4 and Table 5), as well as those earlier discussed for Pb-208 configurations (Table 2 and Table 3) provide a quantitative metric that complements the configuration-by-configuration spectral discussion presented, by summarizing the agreement in peak positions across the CERN Pb-208 and GSI U-238 datasets considered in this work.

A full closure of the remaining gap would require a dedicated sensitivity study (controlled variations of material thickness and density and upstream elements in the geometry) and a more harmonized peak-extraction procedure between simulation and measurement, which is outside the scope of this thesis but naturally follows from the present results.

4.3 SRIM range assessment

The HEARTS deliverable reports, for each tested beam configuration at CERN and GSI, ion ranges in silicon and stainless steel estimated with SRIM [5].

In this thesis, these reference values are used as an external check on the expected penetration of key elements of the PIPS package (for example the 0.5 mm stainless-steel housing) and as a qualitative way to interpret the appearance or suppression of spectral components associated with different trajectory families [12].

Starting from this point, a dedicated SRIM-based layer-by-layer study was performed by evaluating ion ranges and, where needed, residual energies after finite thickness through the main materials of the detector-package stack defined in the GDML model (stainless steel, elastomer, polymer ring, and the 300 μm sensitive silicon region) [12].

The calculations were carried out for the different populations of trajectories to quantify how the additional material budget can affect the ions reaching the active silicon and passing through it.

This SRIM analysis is presented as a complementary penetration study.

4.3.1 SRIM layer-by-layer procedure

For each beam configuration, the SRIM analysis starts from the ion kinetic energy at the DUT, defined at the upstream scoring plane in the Geant4 model, and propagates the ion through a 1D stack of finite-thickness layers corresponding to the GDML detector-package materials encountered by representative trajectory families. For each layer, SRIM stopping/range tables are used to map the incoming kinetic energy to a CSDA-like residual range $R(E)$; after subtracting the layer thickness, the residual kinetic energy is obtained by inverting the same tabulated relation, and the energy loss ΔE is computed layer-by-layer. If the residual range becomes smaller than the layer thickness, the ion is considered stopped upstream of the sensitive silicon region and does not contribute to the expected energy deposition in the 300-µm active volume.

The study is carried out for three representative radii within the beam spot (R = 5 mm) centered on the detector aperture (aperture radius = 4 mm), in order to sample distinct material budgets associated with the "hole" and "package-including" trajectory families. In the present analysis, the selected radii are $r = 0$ mm (minimal material budget), $r = 4.10$ mm (just outside the aperture edge), and $r = 4.80$ mm (more peripheral trajectories still within the beam spot), and the beam direction is set consistently with the simulation convention with the direction vector being $z = (0,0,-1)$.

Using the three representative radii within the beam spot for the mentioned direction, the SRIM layer-by-layer propagation shows how the upstream package budget modifies the residual energy entering the 300-µm sensitive silicon region. At $E_{\mathrm{DUT}} = 387$ MeV/u, all three paths reach silicon, and the energy entering Si decreases from 387 MeV/u (central hole path) to about 359 MeV/u (steel-only path) and 353 MeV/u (steel + elastomer path), consistently with the additional upstream layers outside the aperture. At $E_{\mathrm{DUT}} = 213$ MeV/u, the same hierarchy is observed, with $E_{\mathrm{in,Si}}$ reduced to about 175 MeV/u for $r = 4.10$ and 165 MeV/u for $r = 4.80$, indicating a much stronger sensitivity to small extra thicknesses as the beam energy decreases. At EDUT = 90 MeV/u, SRIM predicts path-dependent threshold behavior: ions along the r=0 mm (hole) path traverse the 300 µm active silicon without stopping (Ein,Si ≈ 90 MeV/u), while ions along the $\mathrm{r} = 4.10$ mm (steel-only) path enter the silicon with 5.7 MeV/u residual energy and stop within the active thickness, and ions along the $\mathrm{r} = 4.80$ mm (steel + elastomer) path stop before reaching the active region. This explains the progressive suppression of package-related spectral components at low DUT energies. This penetration-based picture provides a straightforward qualitative interpretation for

the progressive suppression of package-related spectral components in the low-energy / high-degrader regime, where only the lowest material-budget trajectories are expected to contribute to the deposited-energy spectrum.

All energies are reported as E_{kin}/u at the DUT. SRIM calculations use total ion energy internally and are converted back to MeV/u for reporting.

E_{DUT} [MeV/u]	Path radius	Ions able to reach Si Active Area	Energy entering Si $E_{in,Si}$ [MeV/u]	ΔE_{Si} in 300µm [MeV/u] ([MeV])
387	r = 0mm	Yes	387	5.4 (1115)
387	r = 4.10mm	Yes	359	5.6 (1164)
387	r = 4.80mm	Yes	353	5.6 (1164)
213	r = 0mm	Yes	213	7.4 (1530)
213	r = 4.10mm	Yes	175	8.2 (1711)
213	r = 4.80mm	Yes	165.4	8.4 (1744)
114	r = 0mm	Yes	114	10.6 (2199)
114	r = 4.10mm	Yes	51.8	17.3 (3598)
114	r = 4.80mm	Yes	29.2	23.9 (4972)
90	r = 0mm	Yes	90	12.3 (2571)
90	r = 4.10mm	Stops in Si	5.7	5.7 (1184)
90	r = 4.80mm	Stops before Si	---	---

Figure 36: SRIM layer-by-layer results for Pb-208: for three representative radii (r = 0, 4.10, 4.80 mm) and few exemplary E_{DUT} values, we report whether the ion reaches the active Si, the energy entering the active area $E_{in,Si}$, and the energy deposited in 300 µm ΔE_{Si}.

For U-238, the SRIM layer-by-layer results in the table show that all three representative trajectory families (r = 0 mm, r = 4.10 mm, r = 4.80 mm) are predicted to reach the 300 µm active silicon region at all the considered DUT energies (883, 619, 169, and 141 MeV/u). As expected, the additional package material outside the aperture systematically reduces the energy entering silicon, with $E_{in,Si}$ decreasing from the hole path to the steel-only path and further to the steel + elastomer path at each E_{DUT}. This hierarchy is small at high energy (ex. at 883 MeV/u: 883 → 862 → 855 MeV/u) and becomes much more pronounced at the lowest energy (141 MeV/u: 141 → 84 → 67

MeV/u), indicating a strong sensitivity to small differences in upstream material budget in the low-energy regime even when all paths still remain penetrating.

The same trend is reflected in the predicted energy deposition in the active layer: ΔE_{Si} increases as E_{DUT} decreases, and at fixed E_{DUT} it is larger for trajectories with a larger upstream material budget because those ions enter silicon at lower residual energy (higher stopping power region). At 141 MeV/u, the table predicts ΔE_{Si} of about 2346 MeV for the hole path and up to about 4206 MeV for the r = 4.80 mm path, corresponding to a wide separation in deposited-energy scale between aperture-dominated and package-including trajectories.

E_{DUT} [MeV/u]	Path radius	Ions able to reach Si Active Area	Energy entering Si $E_{in,Si}$ [MeV/u]	ΔE_{Si} in 300µm [MeV/u] ([MeV])
883	r = 0mm	Yes	883	4.3 (1031)
883	r = 4.10mm	Yes	862	4.6 (1098)
883	r = 4.80mm	Yes	855	4.6 (1103)
619	r = 0mm	Yes	619	4.9 (1176)
619	r = 4.10mm	Yes	594	5.3 (1254)
619	r = 4.80mm	Yes	588	5.5 (1298)
169	r = 0mm	Yes	169	8.8 (2109)
169	r = 4.10mm	Yes	120	10.9 (2601)
169	r = 4.80mm	Yes	107	12.0 (2866)
141	r = 0mm	Yes	141	9.9 (2346)
141	r = 4.10mm	Yes	84	12.8 (3038)
141	r = 4.80mm	Yes	67	17.7 (4206)

Figure 37: SRIM layer-by-layer results for U-238: same as for Pb, reporting if ions are able to reach the Si and the values of the energy entering the active area $E_{in,Si}$ and ΔE_{Si} in 300 µm for three trajectories (r = 0 mm, 4.10 mm, 4.80 mm) at the considered E_{DUT} energies.

This penetration picture supports the interpretation of the U-238 deposited-energy spectra as persistently bimodal across the explored energies, with an increasing peak separation towards low E_{DUT}, since the different trajectory families remain present but become more energetically separated as the ions slow down. In contrast with the Pb-208 case, the U-238 table does not show

a configuration where peripheral trajectories stop upstream of the sensitive silicon within the reported energies, so no SRIM-predicted “loss” of an entire trajectory family is expected in this U-238 set.

Chapter 5 – TCAD transient study

5.1 Scope and overview

In this chapter, TCAD simulations performed in the Synopsys Sentaurus environment are used to study the transient electrical response of a PIN diode under a parameterized heavy-ion-like ionization event. The goal is not to reproduce the full experimental readout chain on a one-to-one basis, but to provide a device-level description of signal formation in the time domain and to compare it with CERN transient waveform data used as an experimental reference.

This chapter complements the Monte Carlo analysis presented in the previous chapters. While the GRAS/Geant4 simulations were used to reconstruct the effective beam conditions at the DUT and to interpret the deposited-energy spectra in terms of geometry, materials, and trajectory families, the TCAD study addresses a different and complementary question: how the charge generated in silicon is converted into a transient electrical signal by the internal device physics.

The analysis therefore focuses on the intrinsic current response of the diode, as obtained from the simulated contact current, and on its comparison with a CERN experimental waveform dataset acquired on the same diode type under Pb 500 MeV/n irradiation. The comparison is used here as a time-domain consistency check of the device-level model, with the awareness that the measured waveform reflects the response of the experimental acquisition chain and is therefore not strictly equivalent to the raw TCAD contact current.

Within this framework, the chapter has three main objectives: first, to define a physically plausible TCAD reference model for the PIN diode under reverse bias, second, to analyze the main mechanisms governing transient charge collection in the simulated structure, and third, to assess to what extent the simulated current transient reproduces the main morphological features of the CERN waveform, and where relevant discrepancies remain.

5.2 Device and TCAD setup

The simulated device is a PIN-type diode consisting of a p-type region, a lightly doped intrinsic region, and an n-type region, arranged along the vertical transport direction. The final reference case adopted for the transient study corresponds to the 300 μm detector operated at a reverse bias

of **−60 V**, consistently with the nominal operating condition of the PIPS detector considered in the CERN campaign.

The main structural parameters are:

- **p-region**: length $W_p = 5$ µm, doping $N_a = 1 \times 10^{19} cm^{-3}$
- **i-region (intrinsic)**: length $W_i = 300$ µm, doping $N_i = 1 \times 10^{12} cm^{-3}$
- **n-region**: length $W_n = 5$ µm, doping $N_d = 1 \times 10^{19} cm^{-3}$
- **Lateral width**: L = 100 µm
- **Applied bias voltage**: $V_{bias} = -60\ V$

The main quantity extracted from the simulations is the **total current at the n-contact**, which provides the intrinsic device-level transient current response and is used here for comparison with the CERN waveform dataset, while acknowledging that the measured signal is not strictly identical to the raw simulated contact current [19].

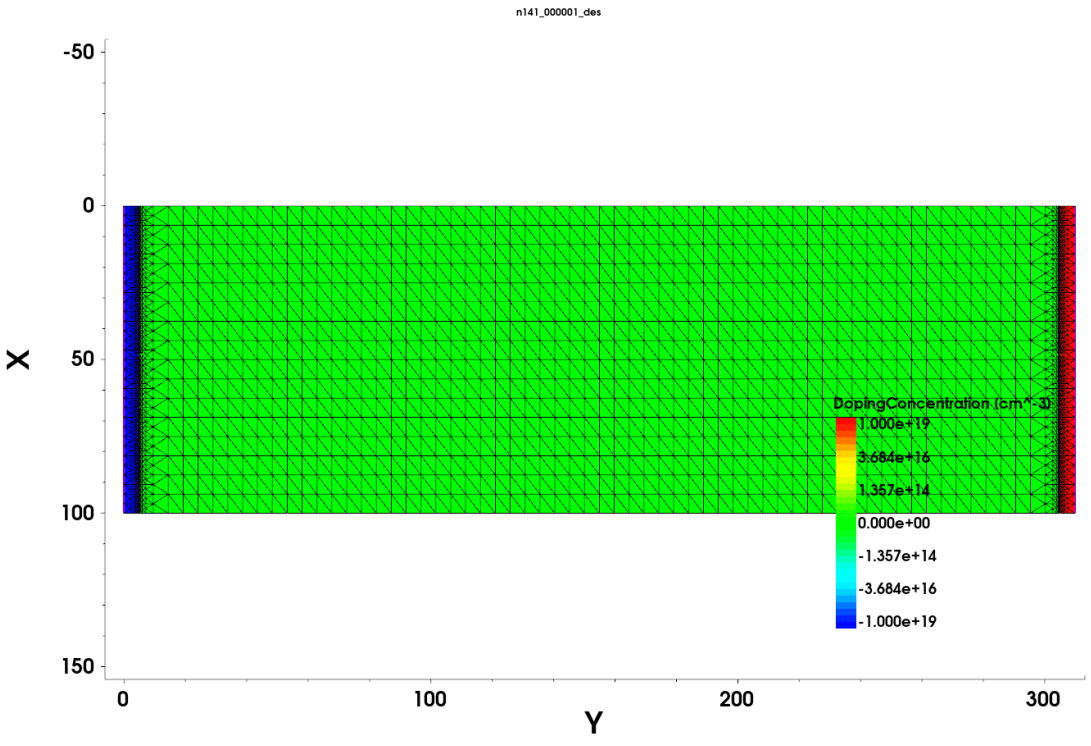

Figure 38: Junction geometry - 2D view with mesh and doping regions (p, i, n). Mesh refined near contacts/junctions to resolve field and concentration gradients.

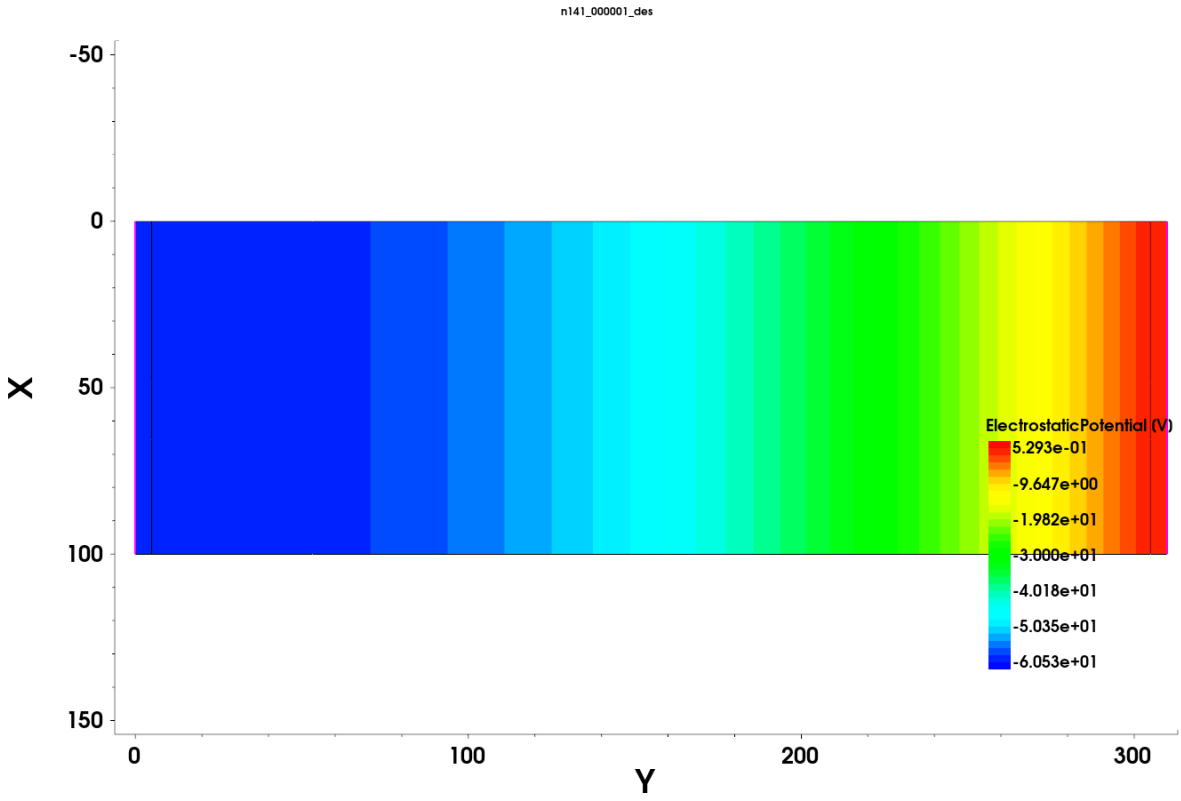

Figure 39: Electrostatic potential distribution in the final TCAD reference configuration (node 141, reverse bias of −60 V). The potential drops monotonically across the diode bulk, consistent with the establishment of the depleted sensitive region used in the transient simulations.

The TCAD simulation was conducted with Synopsys Sentaurus, using SDE for geometry and mesh generation and SDevice for the transient solution. The geometry was constructed in SDE through scripts defining the p, i, n regions, the contacts, and a local mesh refinement strategy using evaluation windows and local mesh-refinement strategy focused on the junction regions. The resulting mesh is sufficiently fine to resolve both the static field distribution and the transient evolution of the carrier densities during the ionization event.

In particular, two rectangular windows centered on the p–i and i–n junctions were introduced, with a half-width of ±0.05 μm around the interface positions, to increase the numerical resolution at points of highest doping/field gradient.

Within these windows, the "refinement size" is set starting from the global parameters x_{max}, y_{max}, x_{min}, y_{min} scaled by a factor of 10, obtaining a local minimum step of 0.05 μm and local maximum steps of 2.5 μm (x-direction) and 0.5 μm (y-direction); the total number of mesh elements is 4384.

5.2.1 Physical models activated

Carrier transport was simulated with the drift-diffusion model, by solving Poisson's equation and the continuity equations for electrons and holes. Carrier mobility was modeled with doping-dependent mobility, while recombination mechanisms included Auger recombination and, in the final reference configuration, also SRH recombination. These physical models provide a standard and sufficiently robust description of carrier transport and recombination in a reverse-biased silicon PIN structure under strong transient charge injection [19].

SRH Recombination

In the SRH model, lifetimes are defined in the parameter file (sdevice.par) with doping dependence through parameters τ_{min}, τ_{max}, N_{ref}, and γ, and with temperature dependence (T_{alpha}, T_{coeff}).
In the present case, $\tau_{max} = 1.0 * 10^{-5} s$ (for electrons) and $3.0 * 10^{-6} s$ (for holes), with $N_{ref} = 1.0 * 10^{16} cm^{-3}$ and γ = 1 (with $\tau_{min} = 0$).

Auger Recombination

Auger recombination is a mechanism by which electrons and holes can recombine, especially when a large amount of charge is created all at once in the silicon immediately after beam passage.
In practice, if the carrier density is high, Auger accelerates the reduction of free charge and this can influence the signal shape, particularly the "tail" portion of the transient.
This choice allows the inclusion of recombination at high carrier densities, which can affect the amplitude and tail of the transient under strong ionization conditions.

HeavyIon Module

The ionization event was introduced through the **HeavyIon** module, which defines a charge-generation source along a track as a function of position and time. In the final reference case, the track is oriented along the device depth direction, with position xloc = 50 µm , trigger time at 50 ns, axial extent of 600 µm, and transverse width parameter $wt_{hi} = 0.3$. The reverse bias for this case is -60V, consistently with the selected 300µm detector operating condition.

The HeavyIon parameters are:

- **LET_f** (Linear Energy Transfer): $2.36 * 10^{-2}\ MeV * \frac{cm^2}{mg}$

- **wt_hi** (track transverse width): 0.3 μm
- **Length** (axial extent): 600 μm
- **Track position xloc**: X = 50 μm
- **Direction**: (x,y) = (0,1) [Horizontal direction in Figure 40, along y]

Charge deposition is applied at time $t = 5 * 10^{-9} s$ and temporal resolution is made finer around the impact through a transient simulation with small minimum step.
The transient was solved with initial time step of 10 ps and maximum time step of 0.1 ns to capture the main transient dynamics without excessive computational cost.

It should be pointed out that the HeavyIon source parameter LET_f should not be interpreted as directly equivalent to the facility LET values reported in the HEARTS deliverable. In the deliverable, LET refers to the beam condition at the silicon surface and is reported in MeV/mg·cm². In the present TCAD setup, instead, LET_f, expressed in pC/μm, is used as an effective source parameter of the Sentaurus HeavyIon model and was calibrated iteratively in order to obtain a simulated collected charge close to the experimental target charge derived from the CERN dataset. For the final reference node, the adopted value is $LET_f = 2.65 * 10^{-2}\, pC/\mu m$ [19].

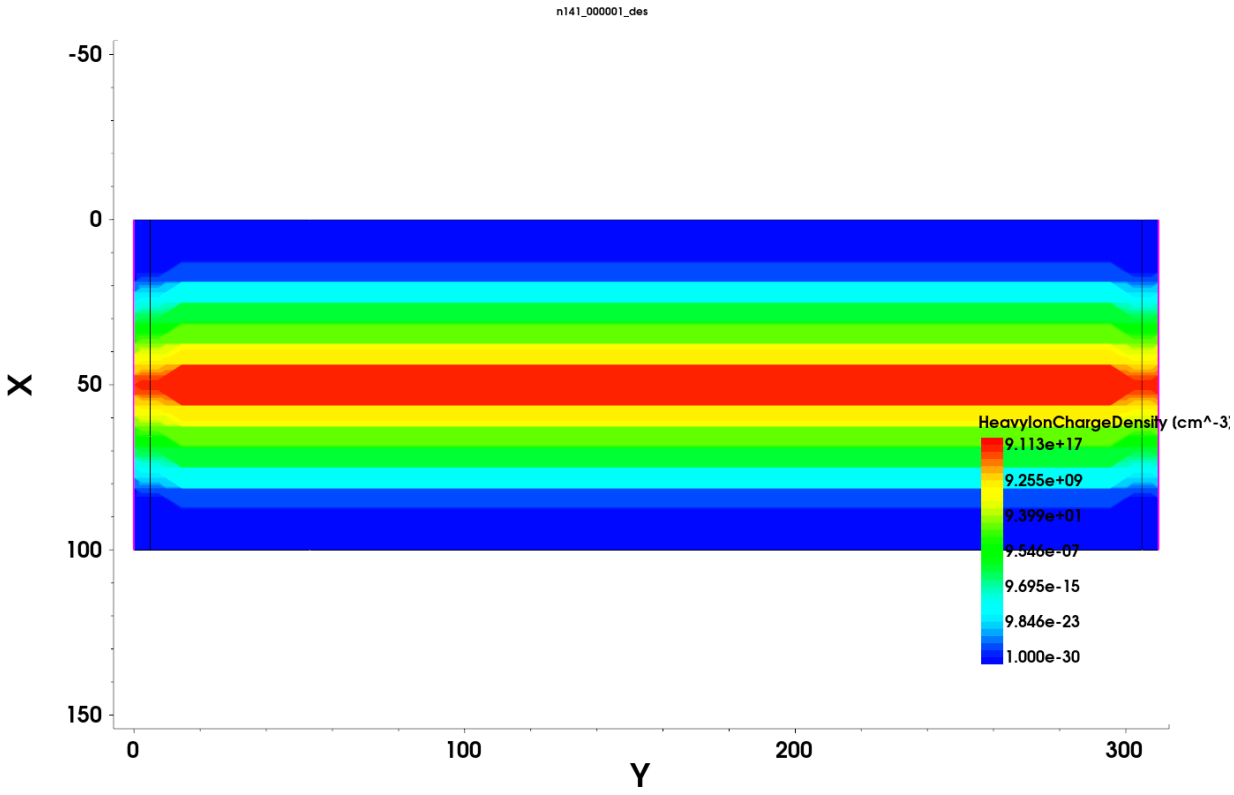

Figure 40: Heavy-ion generated charge-density distribution in the final TCAD reference configuration (node 141, reverse bias of −60 V) for a track with $wt, hi = 0.3\ \mu m$.

5.3 Signal formation (physical picture)

5.3.1 Interaction of Ionizing Radiation with Silicon

The deposited-energy picture discussed in the GRAS part of this thesis must, at device level, be translated into an initial distribution of free charge inside the silicon active region. When an ionizing particle crosses the detector, it loses energy mainly through ionization, generating electron-hole pairs along its path. In silicon, the average energy required to create one electron-hole pair is about 3.6 eV, so the deposited-energy is directly related to the amount of charge initially generated in the sensitive region [19].

In the case of a reverse-biased PIN diode considered here, the intrinsic region (or lightly doped, as in our case at $N_i = 1 * 10^{12}\ cm^{-3}$) constitutes the main detection volume. Thanks to the large thickness of this region and the presence of a significant electric field, the device is capable of efficiently collecting the generated charge, producing a measurable current signal at the contacts. The initial spatial distribution of electron-hole pairs depends on the energy deposition profile of

the particle, which can be idealized as a nearly linear track with a certain extent and transverse width.

5.3.2 Role of Reverse Bias and Electric Field

Application of a reverse bias voltage of −60 V to the PIN diode generates an electric field that extends mainly in the 300 µm-thick intrinsic region. Under full depletion conditions and for very low doping, the field could be approximated as nearly uniform in region i far from the junctions. However, in the present simulation with $V_{bias} = -60\ V$, the electric field is not uniform along the entire thickness of region i (Figure 41), because the device may not be completely depleted, but it is sufficiently extended in the lightly doped central region to support efficient carrier separation and prompt charge collection after ionization.

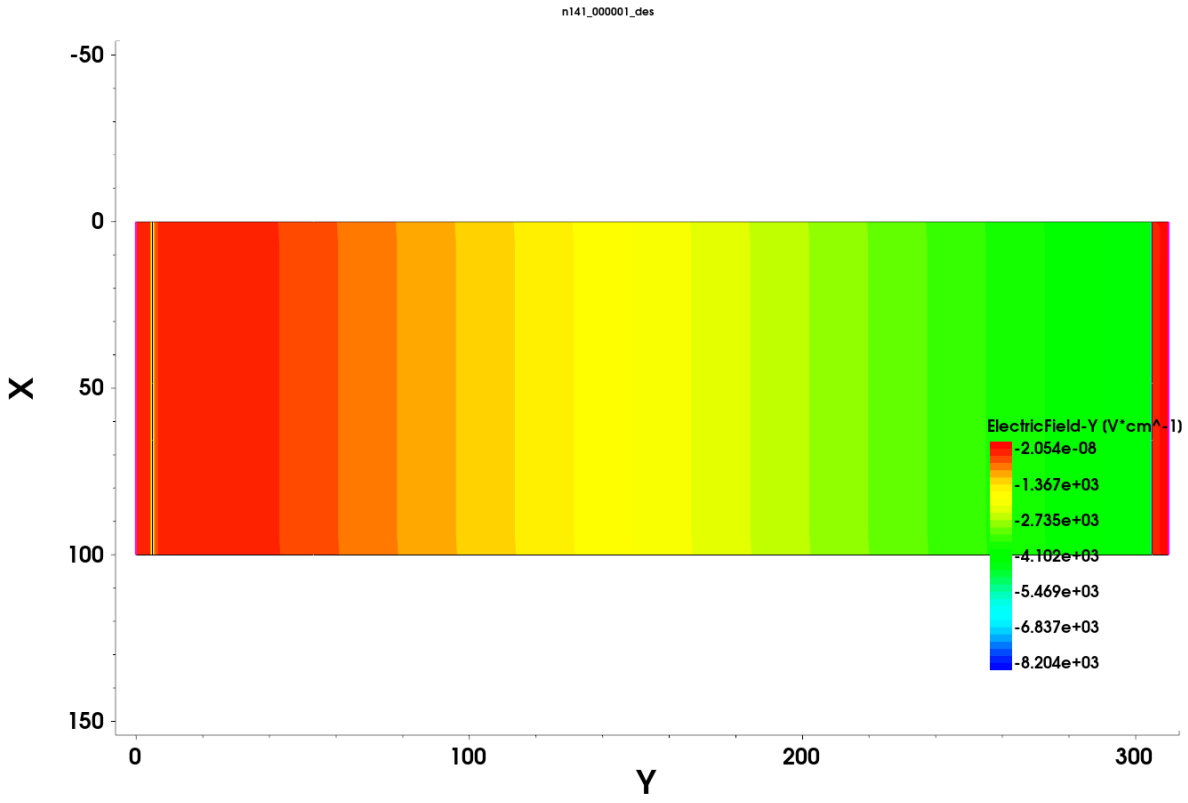

Figure 41: Electric field's y component, in the final TCAD reference configuration (node 141, reverse bias of −60 V). The field extends across the sensitive volume, with higher magnitude near the junction/contact regions, supporting drift-dominated charge collection after ion strike.

The electric field plays a fundamental role in signal formation, since it governs the transport dynamics of the carriers generated by the ionization event. Immediately after charge generation, electrons and holes are accelerated by the field and start moving toward the n-contact and p-contact,

respectively. This ordered carrier motion gives rise to a drift current, which dominates the early part of the transient response. If the electric field were weak or absent, charge collection would rely more strongly on diffusion, leading to longer collection times and a higher probability of recombination. In the reverse-biased PIN structure considered here, the extension of the electric field across the lightly doped central region supports efficient charge separation and fast initial collection, providing the physical basis for the prompt component of the simulated current pulse.

5.3.3 Transport Mechanisms: Drift and Diffusion

The current signal induced in the PIN diode is the combined result, as mentioned earlier, of two carrier transport mechanisms:

- **Drift**, due to the action of the electric field
- **Diffusion**, due to carrier concentration gradients

In the reverse-biased PIN diode considered here, the early part of the signal is mainly associated with drift-driven collection of carriers generated inside regions where the electric field is stronger. This produces the prompt component of the current pulse and largely determines the rise and near-peak behavior of the simulated transient. With the passage of time, as carrier density decreases and a portion of the charge is found in weaker-field regions (for example near the p–i interface, or in lateral regions), the diffusive contribution becomes more relevant. This mechanism is slower and contributes mainly to the decay portion of the signal, namely the so-called "tail" of the transient.
The overall temporal shape of the signal therefore reflects the dynamic equilibrium between these two mechanisms, in addition to recombination processes that progressively reduce the available free charge. As stated, the rise front of the transient is primarily determined by the time required for carriers generated in the intrinsic region to begin drifting under the action of the electric field. This time is typically very short and depends on carrier mobility and field intensity. In devices biased at high voltages, as in the present case, the electron drift velocity can approach saturation velocity, making the rise front particularly rapid. Accurate reproduction of this signal phase represents an important indicator of the correctness of the simulated electric field and the adopted mobility models.
The choice of a PIN structure for radiation detection is motivated by several physical and technological advantages. The wide lightly doped central region provides a large sensitive volume for charge generation and collection following an ionizing event. Moreover, the presence of an

extended electric field under reverse bias supports rapid and efficient carrier separation, limiting recombination effects and improving the temporal response of the detector. These characteristics make the PIN diode particularly suitable for transient-response studies and for device-level comparisons with experimental waveforms, such as those considered in this work.

5.4 CERN dataset and preprocessing

The experimental dataset used in this chapter was provided separately by CERN and contains radiation-induced transients acquired on the Canberra/Vanessa2 diode under Pb 500 MeV/n irradiation. The dataset is organized in a CSV file with columns representing:

- Evt_number: event identifier
- Energy[MeV]: energy deposited in the device for that event
- Transient_0, Transient_1, ..., Transient_405: 406 samples of the measured waveform

The signals are acquired at 1 GHz and expressed in ADC counts. In the present study, Energy[MeV] is interpreted as an event-by-event indicator of the deposited-energy associated with the detected transient and is used to represent the corresponding charge scale in the detector. Since the deposited-energy determines the number of generated electron-hole pairs, it provides a physically meaningful criterion to group events characterized by comparable signal magnitude.

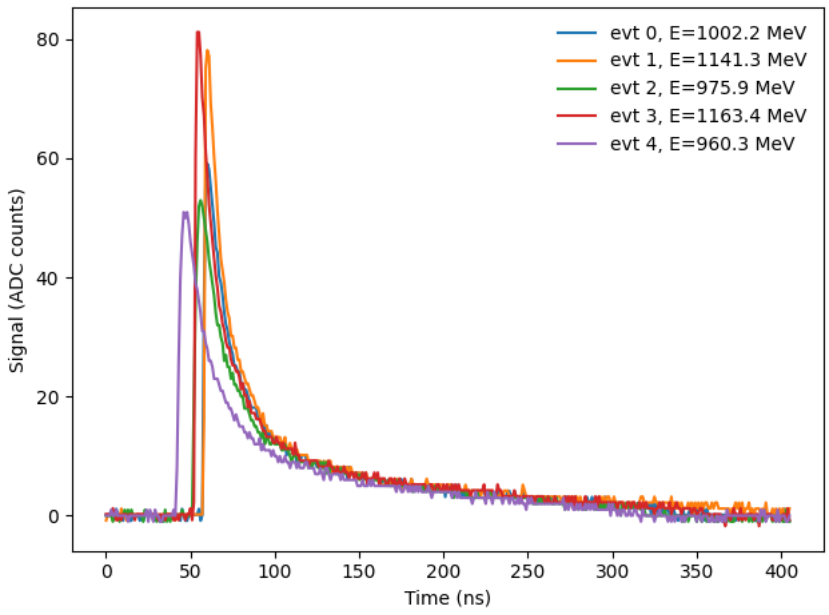

Figure 42: Representative sample of the first 10 individual transient waveforms from the CERN experimental dataset acquired on the Canberra/Vanessa2 diode under Pb 500 MeV/n irradiation.

In TCAD, the integral of the collected current provides a natural device-level quantity related to the collected charge:

$$Q_{\mathrm{col}} = \int I_{\mathrm{TotalCurrent,n}}(t)\, dt$$

Although Energy[MeV] and Q_{col} are not treated here as strictly equivalent observables, they have a relation in defining the signal scale. This distinction is important, because the CERN waveform corresponds to an acquired detector signal expressed in ADC counts, whereas the TCAD output represents the intrinsic current transient of the simulated diode. The comparison is therefore not intended as a point-by-point amplitude validation, but as a controlled comparison between an experimental waveform reference and a device-level transient response.

Preprocessing of CERN Data:

1. **Selection of Energy[MeV] range**: To reduce event-by-event mixing and enable more homogeneous comparisons, the CERN transients are grouped into deposited-energy windows of width ±50 MeV around selected central values. In the present analysis, the bins considered are 1000 ± 50 MeV, 1100 ± 50 MeV, and 1200 ± 50 MeV. These subsets are used to verify whether the qualitative comparison with TCAD remains consistent through the entire dataset.

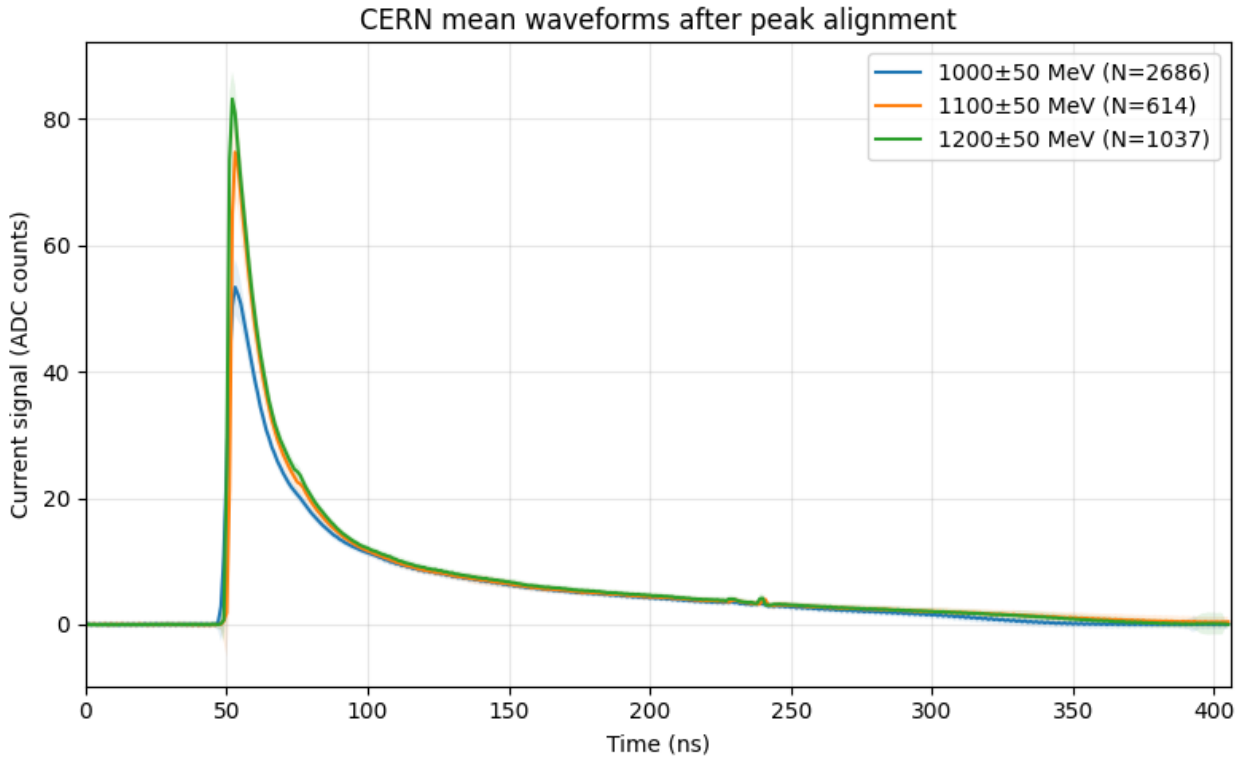

Figure 43: Mean CERN current waveforms for the 1000 ± 50 MeV, 1100 ± 50 MeV, and 1200 ± 50 MeV deposited-energy bins after baseline correction and peak alignment.

2. **Baseline correction**: Before averaging, each experimental transient is baseline-corrected by subtracting the mean value of the first 40 samples. This initial interval was verified to lie before the onset of the transient in almost all events (on average after ~50 samples, and the percentage of events where signal onset falls before sample 40 is approximately 0.5%), so it provides a suitable estimate of the pre-signal baseline. After baseline correction, the sample-by-sample mean waveform is computed for each energy bin, together with the corresponding ±1σ dispersion band, in order to describe both the average transient morphology and its event-by-event variability.

3. **Peak normalization**: In addition to the baseline corrected representation, a peak-normalization is also introduced. After baseline subtraction, each waveform is divided by its absolute maximum, so that the peak amplitude is set to unity. This normalization is used only to compare the local morphology of the signals, especially in the rise and immediate post-peak region, and not to claim direct quantitative equivalence between simulated and experimental amplitudes.

Accordingly, the preprocessing described above yields two complementary representations of the CERN dataset. The first is a baseline-corrected waveform in physical time, used to compare the overall temporal extent and decay behavior of the measured and simulated signals. The second is a peak-normalized waveform, used only for local shape comparison near onset and peak.

5.5 Comparison and results

This section presents the comparison between the final TCAD reference transient and the CERN waveform dataset. The objective is not to establish a point-by-point equivalence between simulated and measured signals, but to evaluate which temporal features of the experimental waveform can be plausibly explained at device level. As will be shown, the comparison indicates partial consistency in the fast signal component, whereas the long-time decay remains significantly different.

Figure 44 shows the intrinsic transient current obtained for the final TCAD reference case (node 141). The waveform exhibits a fast rising component followed by a decaying tail, consistent with a drift-dominated initial charge-collection phase and a subsequent slower relaxation of the device response. This signal is used in the following as the device-level reference for comparison with the CERN waveforms.

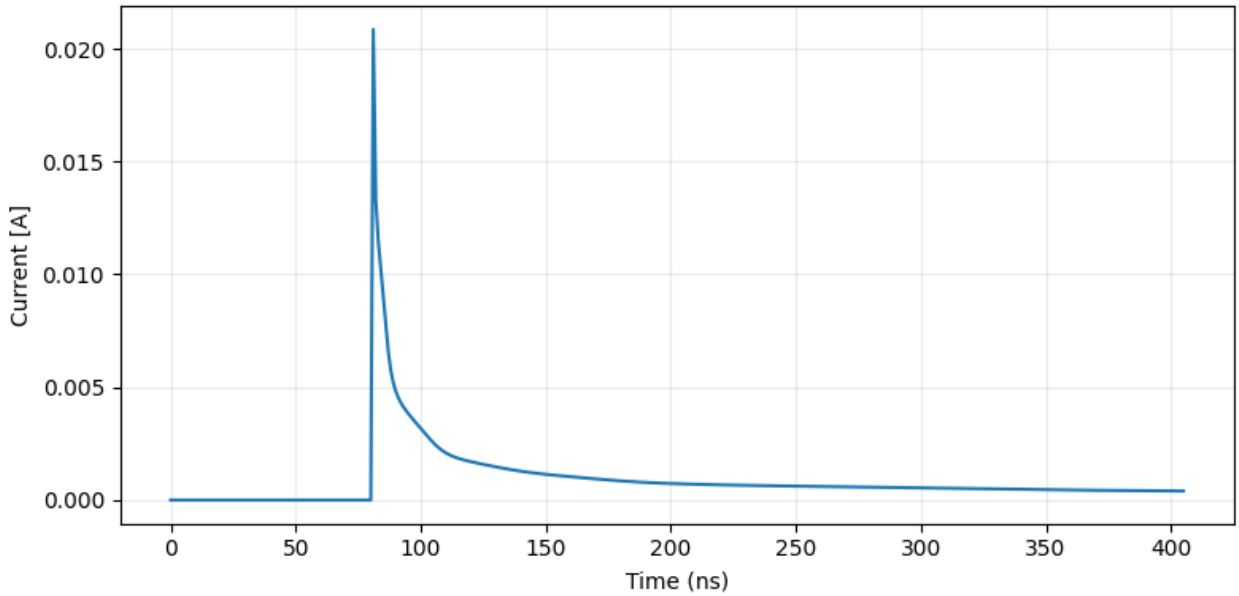

Figure 44: Intrinsic transient current obtained for the final TCAD reference case (node 141).

Before comparing the TCAD transient with the experimental reference, the CERN dataset was examined across the deposited-energy bins defined in Section 5.4. The mean waveforms corresponding to 1000 ± 50 MeV, 1100 ± 50 MeV, and 1200 ± 50 MeV show the same general temporal structure: a fast onset followed by a much longer decaying tail. The main variation across the bins is the signal scale, while the waveform shape remains qualitatively similar. This indicates that, within the considered energy range, the experimental transient shape is sufficiently stable to support a meaningful comparison with a single device-level TCAD reference case.

A further indication of this stability is provided by the inspection of representative individual waveforms from the CERN dataset. Although the raw transients exhibit event-by-event fluctuations in amplitude and small variations in temporal development, they preserve the same characteristic structure already visible in the mean waveforms. This supports the use of averaged waveforms as an experimental reference for the comparison.

Figure 45 shows the peak-centered and peak-normalized comparison between the transient of node 141 and the mean CERN waveform in the 1000 ± 50 MeV interval, together with the corresponding ±1σ band. In this representation, the simulated transient can be aligned with the experimental signal around the onset and peak region. This indicates that the TCAD model captures, at least qualitatively, the existence of a fast signal component compatible with the early part of the measured waveform. However, the agreement remains limited because, already in the immediate post-peak region, the simulated signal decays more rapidly than the CERN mean waveform, and the discrepancy remains relevant until the end of the transient, when the current approaches zero.

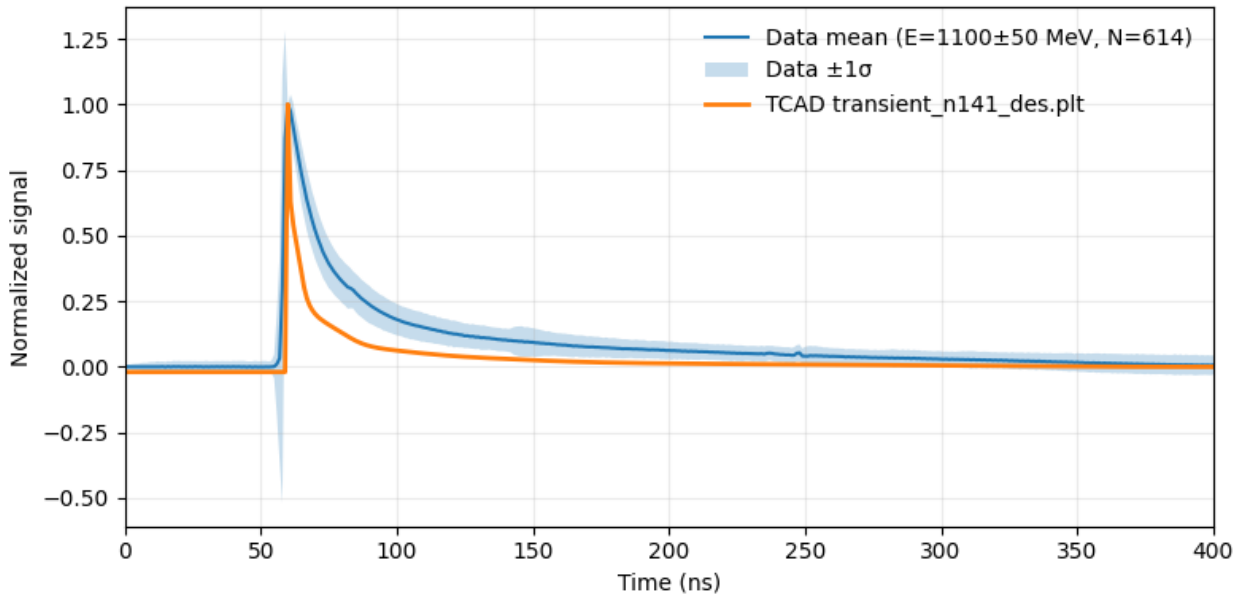

Figure 45: Peak-centered and normalized comparison between the simulated transient of node 141 and the mean CERN waveform for the 1100 ± 50 MeV interval, including the corresponding ±1σ band.

The comparison suggests that the present TCAD configuration reproduces only part of the waveform morphology, mainly in the prompt component close to the signal onset. This result is consistent with the role assigned to TCAD in this thesis, to provide a device-level description of intrinsic signal formation rather than a full reproduction of the acquired detector waveform.

Conclusions

Summary of main results and outlook

This thesis addressed the interpretation of SEE-related measurements in very-high-energy heavy-ion environments by combining two complementary simulation levels: Geant4/GRAS particle-transport simulations and TCAD transient device simulations. The central idea of the work is that the relevant quantity for interpreting the measurements is not the nominal beam setting alone, but the effective particle field at the DUT after transport through degraders, upstream materials, and detector/package geometry. This framework was introduced in the early chapters and then applied throughout the thesis.

The first main result of the thesis is the development of a Geant4/GRAS simulation framework able to reproduce the deposited-energy measurements performed with a packaged silicon PIPS diode in the HEARTS context. The Monte Carlo analysis showed that the measured deposited-energy spectra cannot be interpreted only in terms of nominal beam energy, because geometry and upstream materials strongly affect the energy distribution at the DUT and the resulting spectral structure. In particular, the simulations support the interpretation of the measured spectra in terms of different trajectory families, including contributions from particles crossing the front aperture and from particles traversing additional package material. A central result of this part of the work is that the deposited-energy spectra are strongly shaped by beam transport, upstream materials, and detector-package geometry. This interpretation was enabled by a consistent definition of the effective energy at the DUT through an upstream scoring plane and by a mapping between degrader thickness and residual beam energy at the detector entrance.

The second main result is the TCAD-based device-level analysis of transient signal formation in a reverse-biased PIN structure. In this part of the thesis, the transient current generated by a parameterized heavy-ion ionization event was studied in order to understand how an ionizing track in silicon can produce a measurable time-domain response. The final comparison with the CERN transient dataset showed a partial consistency with the measured waveform. In particular, the comparison indicates a local agreement in the onset and peak region, whereas the experimental

waveform exhibits a significantly extended decay tail than the simulated total current. This result is important because it clarifies the correct role of the TCAD model in the thesis: not to reproduce the full acquired waveform chain, but to identify which part of the measured signal can already be explained at device level.

Taken together, the two simulation levels provide a coherent interpretation of the measurement problem. The Monte Carlo analysis explains how the beamline, degraders, materials, and package shape the deposited-energy distribution at the DUT, while the TCAD analysis shows how a plausible ionization event inside the detector translates into an intrinsic transient current. The combined picture is therefore that both beam transport and device physics are necessary to interpret SEE-related measurements in realistic very-high-energy beam conditions.

Natural extensions of this work include a further refinement of the detector/package model, broader validation across additional beam conditions, and a more complete connection between the intrinsic TCAD current and the experimental waveform chain.

References

[1] E. Normand, “Single-Event Effects in Avionics,” IEEE Transactions on Nuclear Science, vol. 43, no. 2, pp. 461-474, Apr. 1996.

[2] National Academies of Sciences, Engineering, and Medicine, Testing at the Speed of Light: The State of U.S. Electronic Parts Space Radiation Testing Infrastructure. Washington, DC, USA: The National Academies Press, 2018.

[3] M. Kastriotou et al., “Single Event Effect Testing with Ultrahigh Energy Heavy Ion Beams,” IEEE Transactions on Nuclear Science, vol. 67, no. 1, pp. 63-70, Jan. 2020.

[4] A. Waets et al., “Characterization of Fully Fragmented High-Energy Heavy-Ion Beams for SEE Testing Through Measurements and Simulations,” IEEE Transactions on Nuclear Science, vol. 72, pp. 1123–1129, 2025.

[5] S. Gerardin, M. Bagatin, “Validation of beam parameter quality of CERN and GSI infrastructures for testing of electronics”, HEARTS Deliverable D5.2, document identifier HEARTS_D5.2_2025-08-01, WP5, UniPD, Horizon Europe project HEARTS, Aug. 2025

[6] R. García Alía et al., “The HEARTS EU Project and Its Initial Results on Fragmented High-Energy Heavy-Ion Single-Event Effects Testing,” IEEE Transactions on Nuclear Science, vol. 72, pp. 1040-1049, 2025.

[7] M. Bagatin et al., “Characterizing High-Energy Ion Beams With PIPS Detectors,” IEEE Transactions on Nuclear Science, vol. 67, no. 7, pp. 1421-1427, Jul. 2020.

[8] ESCC Basic Specification No. 25100, “Single Event Effects Test Method and Guidelines”, Oct. 2014.

[9] R. A. Reed et al., “Single-event effects ground testing and on-orbit rate prediction methods: The past, present, and future,” IEEE Transactions on Nuclear Science, vol. 50, no. 3, pp. 622-634, Jun. 2003.

[10] Particle Data Group, “Passage of Particles Through Matter,” in Review of Particle Physics, Physical Review D, vol. 110, 2024.

[11] M. Bagatin et al., “Energy Deposition by Ultrahigh Energy Ions in Large and Small Sensitive Volumes,” IEEE Transactions on Nuclear Science, vol. 69, no. 3, pp. 241-247, 2022.

[12] J. F. Ziegler, M. D. Ziegler, and J. P. Biersack, “SRIM—The Stopping and Range of Ions in Matter (2010),” Nuclear Instruments and Methods in Physics Research Section B, vol. 268, no. 11–12, pp. 1818–1823, 2010.

[13] R. García Alía et al., “Fragmented High-Energy Heavy-Ion Beams for Electronics Testing,” IEEE Transactions on Nuclear Science, vol. 70, no. 4, pp. 486–495, Apr. 2023.

[14] M. Buénerd and I. Efthymiopoulos, A High Energy Secondary Beam of Ion Fragments for Instrumental Tests at CERN, CERN-AB-2003-052-ATB, 2003.

[15] Mirion Technologies, “PIPS Detectors: Passivated Implanted Planar Silicon Detectors,” product/technology documentation.

[16] CAEN, “DT5780 – Dual Digital Multi Channel Analyzer (HV & Preamplifier PS),” official product documentation.

[17] S. Agostinelli et al., “Geant4-a Simulation Toolkit,” Nuclear Instruments and Methods in Physics Research Section A, vol. 506, no. 3, pp. 250-303, 2003.

[18] European Space Agency, “GRAS (Geant4 Radiation Analysis for Space),” ESA documentation/project documentation.

[19] Synopsys, “Sentaurus Device: Multidimensional (1D/2D/3D) Device Simulator,” official product documentation.